JEM Journal of Experimental Medicine

ARTICLE

Vision rescue via unconstrained in vivo prime editing in degenerating neural retinas

Huan Qin[1*], Wenliang Zhang[1*], Shiyao Zhang[1*], Yuan Feng[1*], Weihui Xu[1], Jia Qi[1], Qian Zhang[1], Chunxiu Xu[1], Shanshan Liu[1], Jia Zhang[1], Yushuang Lei[1], Wanqin Liu[1], Shuyu Feng[1], Jingjing Wang[1], Xuefei Fu[1], Zifen Xu[1], Ping Li[1], and Kai Yao[1]

Retinitis pigmentosa (RP) is an inherited retinal dystrophy causing progressive and irreversible loss of retinal photoreceptors. Here, we developed a genome-editing tool characterized by the versatility of prime editors (PEs) and unconstrained PAM requirement of a SpCas9 variant (SpRY), referred to as PE^{SpRY}. The diseased retinas of *Pde6b*-associated RP mouse model were transduced via a dual AAV system packaging PE^{SpRY} for the in vivo genome editing through a non-NGG PAM (GTG). The progressing cell loss was reversed once the mutation was corrected, leading to substantial rescue of photoreceptors and production of functional PDE6β. The treated mice exhibited significant responses in electroretinogram and displayed good performance in both passive and active avoidance tests. Moreover, they presented an apparent improvement in visual stimuli-driven optomotor responses and efficiently completed visually guided water-maze tasks. Together, our study provides convincing evidence for the prevention of vision loss caused by RP-associated gene mutations via unconstrained in vivo prime editing in the degenerating retinas.

Introduction

Retinitis pigmentosa (RP) is characterized by progressing retinal degeneration and represents one of the major causes of blindness throughout the world, with an estimated incidence of one in 4,000 human births (Hartong et al., 2006; Verbakel et al., 2018). To date, a variety of mutations in more than 100 genes such as phosphodiesterase 6b (*PDE6b*) have been found to be associated with this devastating inherited retinal disorder (IRD; Daiger et al., 2013; Gagliardi et al., 2019; https://sph.uth.edu/retnet/). The degeneration in diseased retinas begins with the initial dysfunction of dim light-sensing rod photoreceptors distributed throughout the retina, followed by the onset of secondary death of cone photoreceptors present with the highest density at the center of macula and accounting mainly for the color vision, and leads to severe and irreversible deterioration of vision and eventual blindness.

In addition to conventional gene replacement (Jacobson et al., 2015; Russell et al., 2017), the gene editing approaches based on the programmable CRISPR-Cas system have been recently documented to enable targeted genome engineering in gene therapy for the IRDs (Anzalone et al., 2020; Jang et al., 2021; Jo et al., 2019; Maeder et al., 2019; Raguram et al., 2022; Suh et al., 2021; Yu et al., 2017). Adenine base editor (ABE) has been shown to correct a nonsense point mutation at *Rpe65* locus in the retinal pigment epithelium (RPE) of *rd12* mice, a well-known disease model for Leber congenital amaurosis (LCA) in human retinas (Choi et al., 2022; Suh et al., 2021). Considering base editors (BEs) are only capable of targeted conversion of a single base pair (Anzalone et al., 2020; Davis et al., 2022; Gaudelli et al., 2017; Koblan et al., 2021; Komor et al., 2016; Neugebauer et al., 2022; Song et al., 2020), the prime editors (PEs), as the versatile tools able to precisely introduce not only all types of transitions and transversions but also small insertions or deletions (Anzalone et al., 2022; Anzalone et al., 2019), overcome the limitations of BEs and thus provide an alternative solution for in vivo genome editing. In *rd12* mice, PEs are demonstrated to efficiently correct the point mutation in *Rpe65* gene with undetectable off-target effects or indels (Jang et al., 2021), though the versatility of PEs in genome editing has not been fully exploited in this case. It is worth noting that all of the above-mentioned applications target RPE cells while the RP is mainly caused by mutations in genes related to retinal photoreceptors (Daiger et al., 2013; Gagliardi et al., 2019). However, the direct utility of genome editing in the degenerating neural retinas, such as in unhealthy or dying photoreceptors, to rescue vision instead remains limited, although recent reports regarding the introduction of BEs or PEs into wild-type retinas may contribute to our understanding of the applicability of these tools (Chen et al., 2020; Zhi et al., 2022). Unlike the wild-type contexts, in which we

[1]Institute of Visual Neuroscience and Stem Cell Engineering, Wuhan University of Science and Technology, Wuhan, China.

*H. Qin, W. Zhang, S. Zhang, and Y. Feng contributed equally to this paper. Correspondence to Kai Yao: kyao21@outlook.com.

JEM

could choose the optimal protospacer adjacent motif (PAM) for the genome-editing tools tested, the specific locus harboring the mutation in the retinas with inherited diseases does not guarantee an appropriate PAM for Cas proteins and therefore may restrict the targetable scope in the genome (Hille et al., 2018; Jang et al., 2021; Levy et al., 2020; Suh et al., 2021; Zhi et al., 2022). Substantial efforts thus have been made to expand the targeting scope (Anzalone et al., 2019; Cebrian-Serrano and Davies, 2017; Chatterjee et al., 2020a; Chatterjee et al., 2020b; Gao et al., 2017; Hirano et al., 2016; Hu et al., 2018; Kim et al., 2020; Kleinstiver et al., 2016; Kleinstiver et al., 2015; Kleinstiver et al., 2019; Miller et al., 2020; Nishimasu et al., 2018; Walton et al., 2020), and in particular, a near PAM-less SpCas9 variant (SpRY) by using structure-guided engineering has been recently reported (Walton et al., 2020), which comes with an attractive scenario regarding in vivo genome-editing therapies without concerning PAM restriction.

In this study, we developed a genome-editing tool that is characterized by the combination of the versatility of PEs and unconstrained PAM requirement of SpRY, referred to as PE^{SpRY}. This construct, together with its paired gRNAs, was delivered into the neural retinas of *Pde6b*^{rd10} mouse, a well-known RP mouse model, via a split Npu intein–based dual-AAV (adeno-associated virus) system. Liberated from the restrictions caused by the PAM availability and editing types, the PE^{SpRY} system is herein demonstrated to efficiently correct the mutation with a non-NGG PAM (GTG) and with two types of edits (*Pde6b*$^{T\ to\ C}$ and *Pde6b*^{AGA}). Regardless of a complete loss of sight occurring in the age-matched control, the PE^{SpRY} system–elicited genome editing facilitates the apparent preservation of photoreceptors as well as the restoration of compromised PDE6 phosphodiesterase activity, leading to the evident rescue of visual function in *Pde6b*^{rd10} mice, which is substantiated by a detailed electroretinogram (ERG) and behavioral assessments.

Results

PE^{SpRY} system–mediated in vitro genome editing at *Pde6b* locus

The retinal degeneration in *Pde6b*^{rd10} mice is attributed to a change in amino acid composition from arginine residue to cysteine residue at site 560 (R560C) of the protein as a result of an inherited missense mutation from C to T naturally occurring in *Pde6b* gene on the exon 13 (Fig. 1 A; Chang et al., 2007). *Pde6b* encodes a key β subunit of phosphodiesterase (PDE) and exerts a determinant role in initiating rod phototransduction. In *Pde6b*^{rd10} mice, degeneration in outer nuclear layer (ONL) herein started from around postnatal day 16 (P16) with rod dying progressively at the initial phase, followed by the secondary cone death, and leaving only a single row of cell bodies in ONL as early as P60 in comparison with the situations in age-matched wild-type and P14 degenerative contexts (Fig. 1 B; Chang et al., 2007).

Instead of using conventional genome-editing tools with restricted targetable loci due to PAM preferences or with limited editing types able to be installed, we took advantage of an engineered Moloney murine leukemia virus (M-MLV) reverse transcriptase (RT) fused to a near PAM-less variant of *Streptococcus pyogenes* Cas9 (SpRY) with H840A mutation introduced, hereafter referred to as PE^{SpRY} (PE with SpRY nickase), for prime editing with unconstrained PAM availability (Anzalone et al., 2019; Walton et al., 2020). We first in vitro tested the strategy in an engineered mouse Neuro2a cell line carrying the *Pde6b*^{rd10} mutation (referred to as Neuro2a^{rd10}), where the native base C is substituted by T to achieve the same sequence compositions as those in *Pde6b*^{rd10} mice (Fig. 1 A). Based on the previous report (Anzalone et al., 2019), we systematically constructed multiple prime editing guide RNAs (pegRNAs) with single-base resolution around this locus (p1–p14), utilizing recommended lengths of the primer binding site (PBS) and RT template (13–14-nt PBS and 13–15-nt RT templates) in combination with a variety of non-edited strand nicks 51–108-bp away from the target T•A base pair (n1–n7; Fig. 1, C and D; and Tables S1 and S2). Three regular types of targeted edits at or around the locus from the most common single point edit to the combination edits, including a single nucleotide substitution (T to C, namely an edit back to wild-type, herein referred to as *Pde6b*$^{T\ to\ C}$), a silent mutation with double substitutions (TGC to AGA, no change in amino acid composition relative to wild-type, named as *Pde6b*^{AGA}), as well as combination edits with a small insertion and substitution (AC insertion and T to C, named as *Pde6b*$^{ACins,\ TtoC}$; Fig. S1 A), were assayed and the percentage of correct edits and indels were quantified by high-throughput deep sequencing.

We first tested the single nucleotide substitution (*Pde6b*$^{T\ to\ C}$), which is also the major type of gene correction performed in vivo later. The quantification of the percentage of edited versus total DNA for each pair of pegRNA and ngRNA (nicking gRNA) indicated that PE^{SpRY} efficiently edited the targeted locus with a broad targeting scope acquired due to the nearly completely relaxed PAM requirement and that the highest editing efficiency was up to 35.02 ± 0.91% for pair of p5 and n3 (designated as p5n3; Fig. 1 E). Four of the pairs with relatively higher efficiencies, namely p5n2 (31.22 ± 1.87%), p5n3, p4n4 (27.12 ± 0.87%), and p9n6 (24.77 ± 0.49%), were selected for the further pegRNA optimization of RT template and PBS lengths (Fig. 1, F and G; Fig. S1, B–G; and Table S3). As a consequence, the editing efficiencies were considerably enhanced when the RT templates were 12 nt (Fig. 1 F) and PBS lengths were 14 nt, respectively (Fig. 1 G), and further rose to 63.76 ± 0.94% when tested for p5n3 with the optimized 12-nt RT template and 14-nt PBS (Fig. 1 H). In particular, the selected pair of pegRNA and ngRNA (p5n3), along with the optimized RT templates (12 nt) and PBS (14 nt), was also amenable to efficiently installing diverse mutation types including *Pde6b*^{AGA} (55.24 ± 1.14%) and *Pde6b*$^{ACins,\ TtoC}$ (55.46 ± 1.30%) despite the slight alteration in base composition of RT templates (Fig. 1 H, Fig. S1, H–J; and Table S4). Of note, the indels observed were lower than 0.2% in the samples tested, suggesting the applicability of PE^{SpRY} system in installing the desired edits (Fig. 1, E–H; and Fig. S1, B–G). To highlight the applicability of this strategy, we sought to assess whether the conventional prime editor, namely PE^{SpCas9} (PE with SpCas9 nickase), was capable of introducing the desired edits at this locus (Fig. S1, K and L). Unfortunately, we did not detect any edited DNA even if all of the available canonical PAMs neighboring the targeted

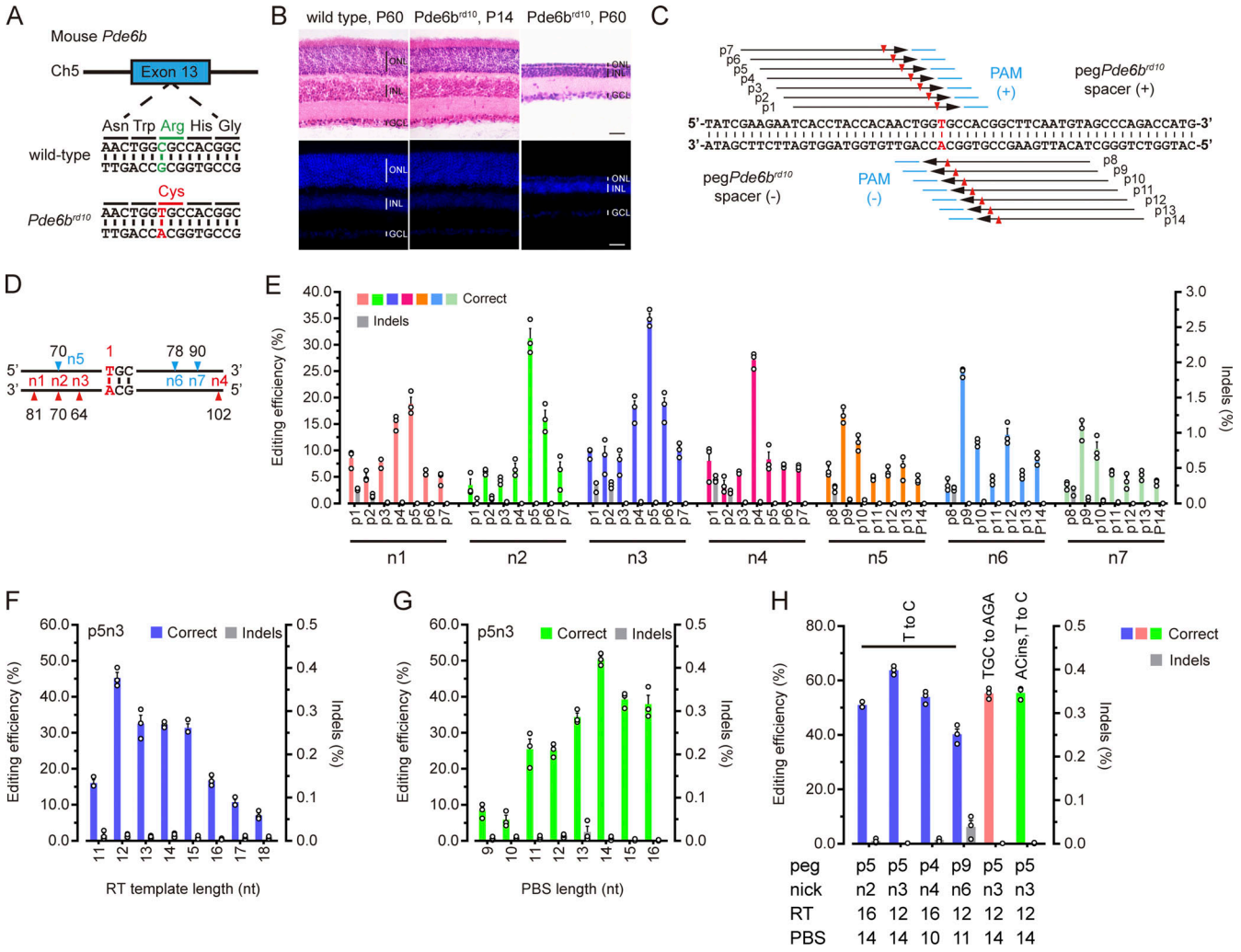

Figure 1. **PE^{SpRY} system–mediated in vitro genome editing at mouse *Pde6b* locus. (A)** The *Pde6b*^{rd10} mouse model has an inherited missense mutation from C to T naturally occurring in the *Pde6b* gene on the exon 13, changing an arginine (green) to a cysteine (red). **(B)** Representative histological images of wild-type retina at P60 and *Pde6b*^{rd10} retina at P14 as well as P60, respectively. Upper panel: H&E staining. INL, inner nuclear layer; GCL, ganglion cell layer. Scale bars, 20 µm. **(C)** 14 pegRNAs (p1–p14) are designed with single-base resolution around the locus (T•A) in an engineered Neuro2a cell line with rd10 mutation (referred to as Neuro2a^{rd10}). p1–p7 and p8–p14 have their nick sites on the sense and antisense strands, respectively. The target T•A base pair is highlighted in red. pegRNA nick sites are indicated as red triangles. PAMs are indicated in blue. **(D)** Selected non-edited strand nicks (n1–n7). Nick sites on the sense and antisense strands are indicated as blue and red, respectively. Numbers indicate the distances (bp) of nick sites from T•A. **(E)** Editing efficiency of correct edits and indels for p1–p7 and p8–p14 with a variety of non-edited strand nicks (n1–n7). **(F and G)** Editing efficiency of correct edits and indels for p5 and n3 combination (designated as p5n3) with varying PBS (F) or RT template (G) lengths. **(H)** Editing efficiency of correct edits and indels for *Pde6b*$^{T\ to\ C}$, *Pde6b*^{AGA}, and *Pde6b*$^{ACins,\ TtoC}$ with p5n2, p5n3, p4n4, or p9n6 combinations and optimized PBS and RT template. Representative data in E–H are presented as mean ± SEM; *n* = 3 independent biological replicates. All experiments were independently performed at least three times to ensure repeatable results.

locus were selected for the test (only high-throughput sequencing result for PE^{SpCas9} p1 was shown; Fig. S1, K and L). We speculated that such a low efficiency was likely due to, at least in part, the sparsely and somewhat distantly distributed NGG PAMs required for PE^{SpCas9}, which results in long RT templates (such as PAM3–7) or the incompatibility between available protospacers/PAMs and their Cas9 counterpart even if the PAMs are adjacent to the targeted T•A pair (PAM1 and 2; Fig. S1 K and Table S5). Of particular interest, one of the protospacers tested, PE^{SpCas9} p1, was not found to efficiently edit the target locus even if it did with a relatively low efficiency when used for PE^{SpRY} (p7 pegRNA), suggesting extended compatibility between the PE^{SpRY} and its pegRNAs at this specific locus. Collectively, PE^{SpRY} system demonstrated its seemingly sophisticated potential for in vitro installation of desired edits at *Pde6b* locus without constraints from PAMs and editing types.

PE^{SpRY} system–elicited photoreceptor preservation in *Pde6b*^{rd10} mice

Having demonstrated the potential that desired combination edits could be installed into the genome through PE^{SpRY} system without stringent PAM restriction, we were motivated to further evaluate whether the strategy could be amenable to the in vivo mutation correction in *Pde6b*^{rd10} mice. Since p5n3 with

optimized RT template (12 nt) and PBS (14 nt) has shown the best performance in installing desired edits in Neuro2a^{rd10} cells, we would mainly utilize this setup for two types of targeted correction in *Pde6b*^{rd10} mice. One is regular single nucleotide substitution (from T in *Pde6b*^{rd10} to C in wild-type, hereafter referred to as *Pde6b*$^{T\ to\ C}$) and the other one is a silent edit (relative to wild-type context) from TGC in *Pde6b*^{rd10} to AGA (uniformly referred to as *Pde6b*^{AGA}), which still encodes Arg residue as wild-type locus (Fig. S2 A). As for the delivery, we exploited a split Npu intein–based dual-AAV system widely used for packaging large size of genome editors (Chen et al., 2020; Chew et al., 2016; Levy et al., 2020; Zhi et al., 2022), and the splitting site at 713–714 of SpRY protein would guarantee the accommodation of PE^{SpRY} in AAV vectors (Fig. S2 A).

Pde6b^{rd10} mice were subretinally injected at P14, a time point right before the onset of rod degeneration, with AAV vectors packaging split PE^{SpRY} and g*Pde6b*-GFP (hereafter referred to as PE^{SpRY} and g*Pde6b*) or with those packaging split PE^{SpRY} and gScrambled-GFP (hereafter referred to as PE^{SpRY} and gScrambled) as a control (Fig. 2 A and Fig. S2 A). The immunoblotting assay of retinas 3 wk after injection indicated that PE^{SpRY} was clearly expressed and spliced in the retinas transduced with AAV vectors packaging the transgenes (Fig. S2 B). The retinas were then harvested and assayed at P120 when photoreceptor death is nearly completed (Fig. 2 A). Since GFP was coexpressed with PE^{SpRY} system, the transduction efficiency would be conveniently visualized by GFP. Compared with the undetectable fluorescence in the untransduced retinas (Fig. S2, E and F), the abundant expression of GFP in the transduced retinas further suggested the reliability and high efficiency of the delivery strategy (Fig. S2, C and D). The percentage of GFP$^+$ cells was quantified by flow cytometry and up to averaging 54.05 ± 0.82 and 45.95 ± 0.66% at P35 and P120, respectively (Fig. S2 G). The editing frequencies were up to averaging 76.34 ± 1.10 and 40.86 ± 0.89% with indels of 0.14 ± 0.02% (Data S1 A) and 0.04 ± 0.01% in the sorted GFP$^+$ and total cells of retinas transduced with vectors installing the edit from T to C, namely *Pde6b*$^{T\ to\ C}$ (Fig. 2 B and Fig. S2 H). The editing activities for p5n3 appeared more efficient in comparison with an editing frequency of 67.06 ± 0.16% and an indel of 0.07 ± 0.01% for p5n2 (Fig. 2 B), and those receiving vectors installing *Pde6b*^{AGA} demonstrated editing activities reaching an average of 69.92 ± 0.9 and 60.59 ± 0.4% with the indels of 0.19 ± 0.02% (Data S1 B) and 0.12 ± 0.02% for p5n3 and p5n2, respectively (Fig. 2 B; Fig. S2, I and J; and Table S6). By contrast, the control vectors did not elicit any editing at the target locus (Fig. S2 K). In the meantime, the editing activities exhibited higher frequencies in retinas harvested at P120 than those in retinas harvested at P35 (Fig. 2 B and Fig. S2 L) likely because most of photoreceptors left at P120 have been subjected to editing. Notably, no apparent editing activities were found at the sites of ngRNA (Data S1, C and D). As a consequence of the correction, the expression of PDE6β was restored significantly since P21 and rose to around 75% level of wild-type at P60 (Fig. 2, C and D), in striking contrast to the PE^{SpRY} and gScrambled-treated *Pde6b*^{rd10} control where PDE6β level decreased to rarely detectable level since P28 (Fig. 2 D and Fig. S2 M). The immunoblotting of Rhodopsin, a rod-specific marker, further validated rod cell preservation in the gene-corrected retinas (Fig. S2 N). As for off-target editing, an unbiased circularization for in vitro reporting of cleavage effects by sequencing (CIRCLE-seq) assay indicated that no significant off-target activities were detectable for treated retinas harvested at 1 or 4 mo after injection (Fig. S2, O and P).

The quantitative assay on the retinal sections indicated that the ONL was up to averaging 53.80 ± 4.8 µm at the thickest position in the *Pde6b*$^{T\ to\ C}$ mice (Fig. 2 E). This thickness was close to that in wild-type mice (averaging 62.70 ± 1.8 µm) while in striking contrast to the situation in the PE^{SpRY} and gScrambled-treated *Pde6b*^{rd10} control where the ONL thickness dropped to averaging <6 µm (Fig. 2 E and Fig. S3, A–C). At most peripheral regions, the ONL thickness in the *Pde6b*$^{T\ to\ C}$ mice was over 20 µm, approximately half of the thickness in wild-type mice, irrespective of the single row of photoreceptor cell bodies left in the *Pde6b*^{rd10} control (Fig. 2, E, G, and K). To assess whether the photoreceptors were preserved upon mutation correction, we assayed the retinas with Rhodopsin antibody on the retinal sections (Fig. S3 D). Compared with the complete loss of rod photoreceptors and significantly compromised retinal morphology occurring in the *Pde6b*^{rd10} control mice treated with PE^{SpRY} and gScrambled (Fig. 2, F, G–J, O, and Q–S), rod photoreceptors instead remained preserved and the defined stratums of ONL were relatively well maintained in the *Pde6b*$^{T\ to\ C}$ retinas (Fig. 2, F, K–O, and T–V) with a Rhodopsin immunofluorescence intensity of nearly 70% of those in wild-type retinas (Fig. 2, F and O). Of note, no Rhodopsin signals were found in the absence of GFP signals in the *Pde6b*$^{T\ to\ C}$ mice (Fig. 2, K–N), suggesting a close correlation between the rescue of photoreceptors and PE^{SpRY} system–elicited genome editing visualized via GFP signals. This speculation was further supported by a closer examination of the region where Rhodopsin and GFP signals tapered down steadily and concomitantly indeed (Fig. 2, P and W–Y). The prevention of photoreceptor degeneration by PE^{SpRY}-elicited genome editing was examined further through immunohistochemistry on retinal sections with antibodies against Pde6β, Gnat1 (rod marker), Recoverin (rod marker), Synaptophysin (photoreceptor presynaptic marker), as well as PKCα (rod bipolar marker). Compared with fairly weak or nearly undetectable signals of Pde6β, Gnat1, and Recoverin in *Pde6b*^{rd10} control treated with PE^{SpRY} and gScrambled (Fig. 3, A, C, E, F, and J), the localizations of these rod-phototransduction relevant proteins were well sustained in the preserved photoreceptors from the *Pde6b*$^{T\ to\ C}$ retinas (Fig. 3, B, D, and G), which was essentially in line with the profiles in wild-type (Fig. S3, E, G, H, J, and K), and their levels were around or over half levels of those in wild-type mice (Fig. 3, E and J). The pattern of Synaptophysin and PKCα demonstrated the dynamic changes of synapses between photoreceptors and bipolar cells. In the *Pde6b*^{rd10} control treated with PE^{SpRY} and gScrambled, the photoreceptor axons and rod bipolar dendrites have been significantly degenerating with Synaptophysin sparsely distributed in photoreceptor axon terminals (Fig. 3, K and M) and with negligible rod bipolar dendritic terminals indicated by PKCα (Fig. 3, H and J). By contrast, both of them in the *Pde6b*$^{T\ to\ C}$ context (Fig. 3, I, J, L, and M) appeared essentially similar to those in wild-type and reached ∼50% levels of those in wild-type mice (Fig. S3, F, H, I, and K) with the exception of additional PKCα staining across

JEM

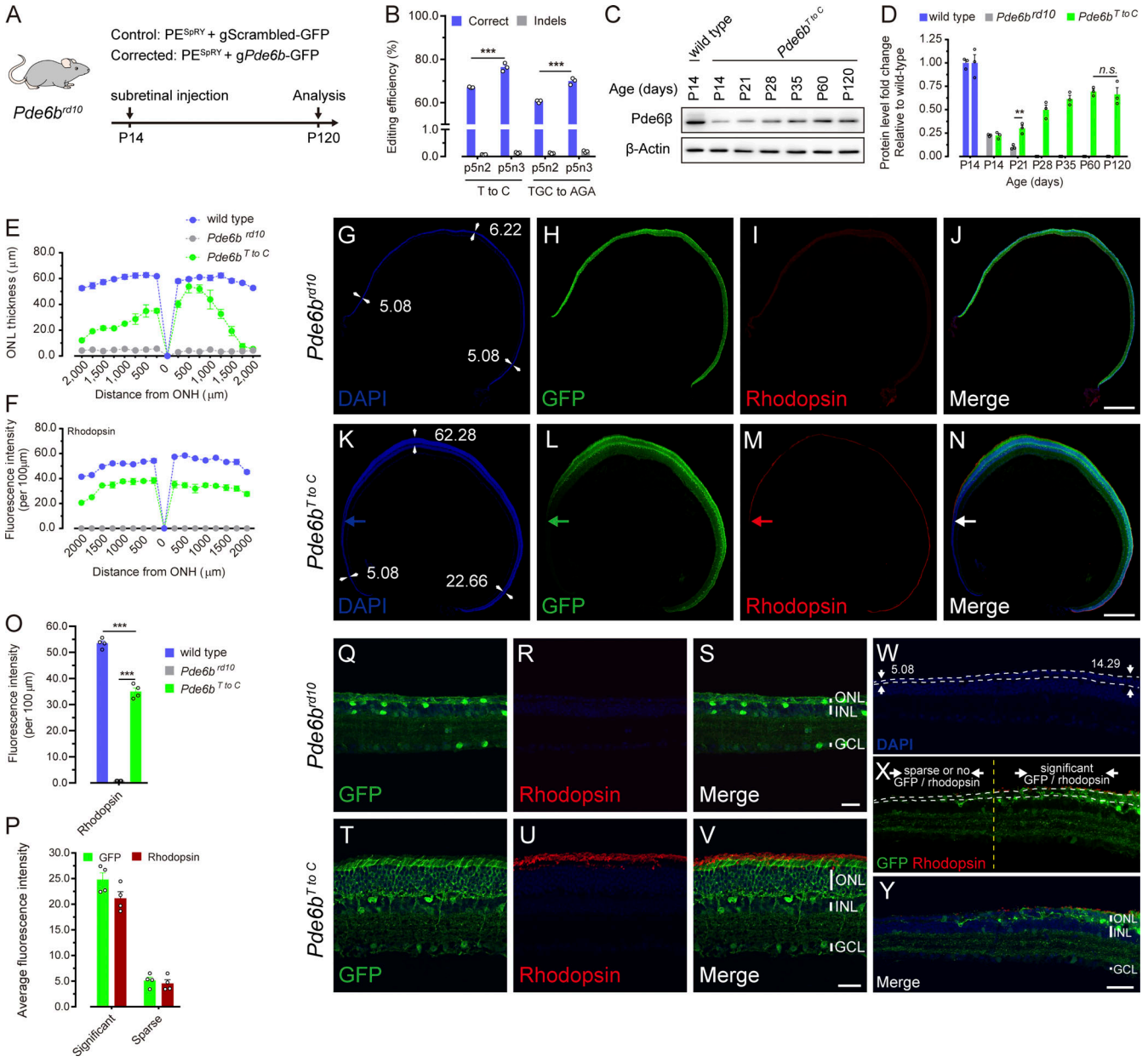

Figure 2. **Photoreceptor preservation in the *Pde6b*^{rd10} mouse retinas treated with PE^{SpRY} system and *gPde6b*. (A)** Experimental outline of the in vivo studies. Unless otherwise stated, retinas were harvested for assays at P120. **(B)** Frequencies of correct edits and indels in the total sequencing reads for *Pde6b*$^{T\ to\ C}$ and *Pde6b*^{AGA} editing with p5n3 or p5n2 combinations and with the optimized PBS and RT template lengths in sorted GFP$^+$ retinal cells. Representative data are presented as mean ± SEM; *n* = 3 independent biological replicates. Two-way ANOVA tests with Tukey's multiple comparisons. ***, P < 0.001. **(C and D)** Pde6β protein is restored to a considerable level in *Pde6b*$^{T\ to\ C}$ retinas at P120. Pde6β proteins were examined for retinal extracts from wild-type and *Pde6b*$^{T\ to\ C}$ retinas at different ages. Representative immunoblotting images for Pde6β and β-Actin are shown in C and the relative Pde6β protein levels of wild-type, *Pde6b*^{rd10}, and *Pde6b*$^{T\ to\ C}$ retinas at different ages are quantified in D. Data are presented as mean ± SEM; *n* = 3 independent biological replicates. Two-way ANOVA tests with Tukey's multiple comparisons. **, P < 0.01; n.s., P > 0.05. **(E)** Thickness of the ONL of wild-type (blue), *Pde6b*^{rd10} (gray), and *Pde6b*$^{T\ to\ C}$ mice (green) at P120. Representative data are presented as mean ± SEM; *n* = 3 independent biological replicates. **(F)** Fluorescence intensities of Rhodopsin immunohistochemistry of wild-type (blue), *Pde6b*^{rd10} (gray), and *Pde6b*$^{T\ to\ C}$ mice (green) at P120. Representative data are presented as mean ± SEM; *n* = 3 independent biological replicates. **(G–N)** Rod photoreceptor preservation in the *Pde6b*$^{T\ to\ C}$ mice. The retinas from *Pde6b*^{rd10} control mice (G–J) or *Pde6b*$^{T\ to\ C}$ mice (K–N) were sectioned and raised for Rhodopsin antibody. Representative images are shown. Blue, DAPI; green, GFP; red, Rhodopsin. Numbers in G and K present the thickness of the regions indicated with white arrows. The horizontal arrows in K–N indicate the positions where GFP and Rhodopsin signals attenuate concomitantly. Scale bars, 300 μm. **(O)** Fluorescence intensities of Rhodopsin immunohistochemistry of wild-type, *Pde6b*^{rd10}, and *Pde6b*$^{T\ to\ C}$ retinal sections were quantified. Representative data are presented as mean ± SEM; *n* = 4 independent biological replicates. One-way ANOVA tests with Tukey's multiple comparisons. ***, P < 0.001. **(P)** Changes of Rhodopsin signals with GFP in *Pde6b*$^{T\ to\ C}$ retinas were quantified. Representative data are presented as mean ± SEM; *n* = 4 independent biological replicates. **(Q–V)** Examination of Rhodopsin immunohistochemistry with higher magnification for *Pde6b*^{rd10} control (Q–S) and *Pde6b*$^{T\ to\ C}$ (T–V) retinal sections. Representative images are shown, and the fluorescence intensities are quantified in O. INL, inner nuclear layer; GCL, ganglion cell layer. Scale bars, 20 μm. **(W–Y)** GFP and Rhodopsin signals attenuate steadily and concomitantly in *Pde6b*$^{T\ to\ C}$ mice. Numbers in W present the thickness of the region indicated with arrows. The ONL is indicated with white dashed lines. The yellow vertical line in X

demonstrates the position where GFP and Rhodopsin signals attenuate concomitantly. Representative images are shown and the fluorescence intensities are quantified in P. Scale bars, 20 µm. All of *Pde6b*^{rd10} control retinas were treated with PE^{SpRY} and gScrambled. All experiments were independently performed at least three times to ensure repeatable results. Source data are available for this figure: SourceData F2.

the OPL (Fig. 3 I), which is likely to represent a compensatory mechanism for the degenerating photoreceptor axons before the corrected Pde6β is expressed.

Since rod death is followed by secondary cone death in the *Pde6b*^{rd10} mice, we further evaluated whether cone photoreceptors were preserved by PE^{SpRY}-elicited genome editing. Cone photoreceptors herein were visualized with peanut agglutinin (PNA), a well-known marker for all cone photoreceptor subtypes, through immunohistochemistry. Irrespective of the barely detectable staining in the *Pde6b*^{rd10} control mice treated with PE^{SpRY} and gScrambled (Fig. 4, A–D and I), the PNA levels exhibited over half of those in wild-type mice in the *Pde6b*$^{T\ to\ C}$ context, and the profile, similar to Rhodopsin, indicated a close correlation with GFP signals (Fig. 4, E–I). A closer examination further evidenced that PNA only presented sparsely and was undetectable in most regions in the *Pde6b*^{rd10} control mice treated with PE^{SpRY} and gScrambled (Fig. 4, J–L and P), whereas PNA appeared bushy and erect in the *Pde6b*$^{T\ to\ C}$ mice (Fig. 4, M–P). The concomitant decline of PNA and GFP signal intensities further supported that the cone preservation was a consequence of PE^{SpRY}-elicited genome editing (Fig. 4, Q–T).

In the meantime, we compared the preservative effects in the *Pde6b*$^{T\ to\ C}$ context treated at P14 and P21. Despite the much faster degeneration process in the *Pde6b*^{rd10} mice compared with humans, the editing efficiency and rescue effect were significant in *Pde6b*$^{T\ to\ C}$ retinas treated at P21 with an editing frequency averaging 41.91 ± 1.29% (Fig. S3, L and M) and a Rhodopsin fluorescence intensity of less than half of those in the retinas treated

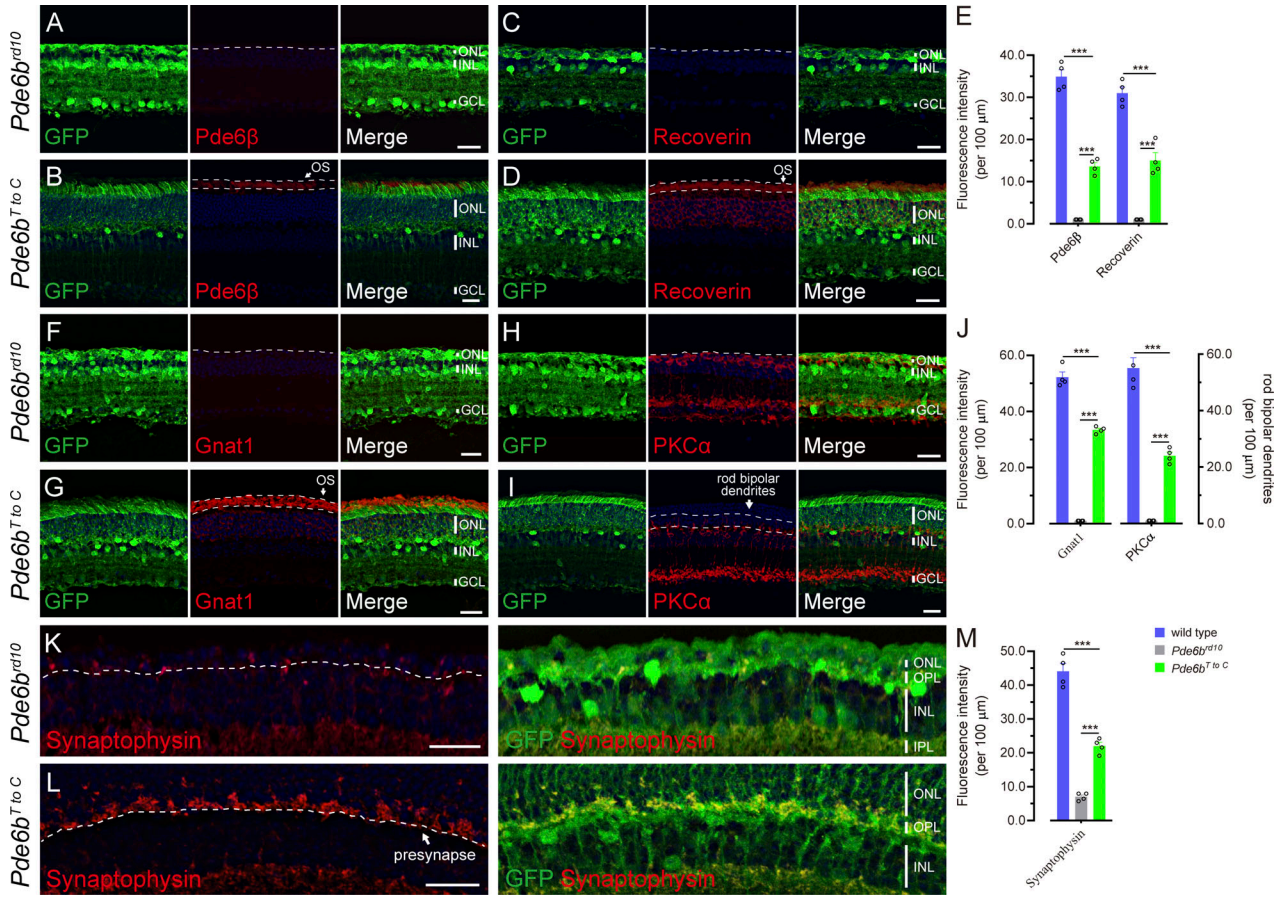

Figure 3. **Rod photoreceptors are significantly preserved in the *Pde6b*^{rd10} mouse retinas treated with PE^{SpRY} system and g*Pde6b*. (A–M)** The retinas from *Pde6b*^{rd10} control (A, C, F, H, and K) or *Pde6b*$^{T\ to\ C}$ (B, D, G, I, and L) mice were sectioned and examined with Pde6β (A and B), Recoverin (C and D), Gnat1 (F and G), PKCα (H and I), and Synaptophysin (K and L) antibodies for immunohistochemistry. Dash lines indicate the segments of photoreceptors in A–D, F, and G, rod bipolar dendrites in H and I, and presynapse of photoreceptors in K and L, respectively. Representative images are shown and the fluorescence intensities are quantified in E, J, and M. Representative data are presented as mean ± SEM; *n* = 4 independent biological replicates. One-way ANOVA tests with Tukey's multiple comparisons. ***, P < 0.001. OS, outer segment; OPL, outer plexiform layer; INL, inner nuclear layer; IPL, inner plexiform layer; and GCL, ganglion cell layer. Scale bars, 20 µm. All of *Pde6b*^{rd10} control retinas were treated with PE^{SpRY} and gScrambled. All experiments were independently performed at least three times to ensure repeatable results.

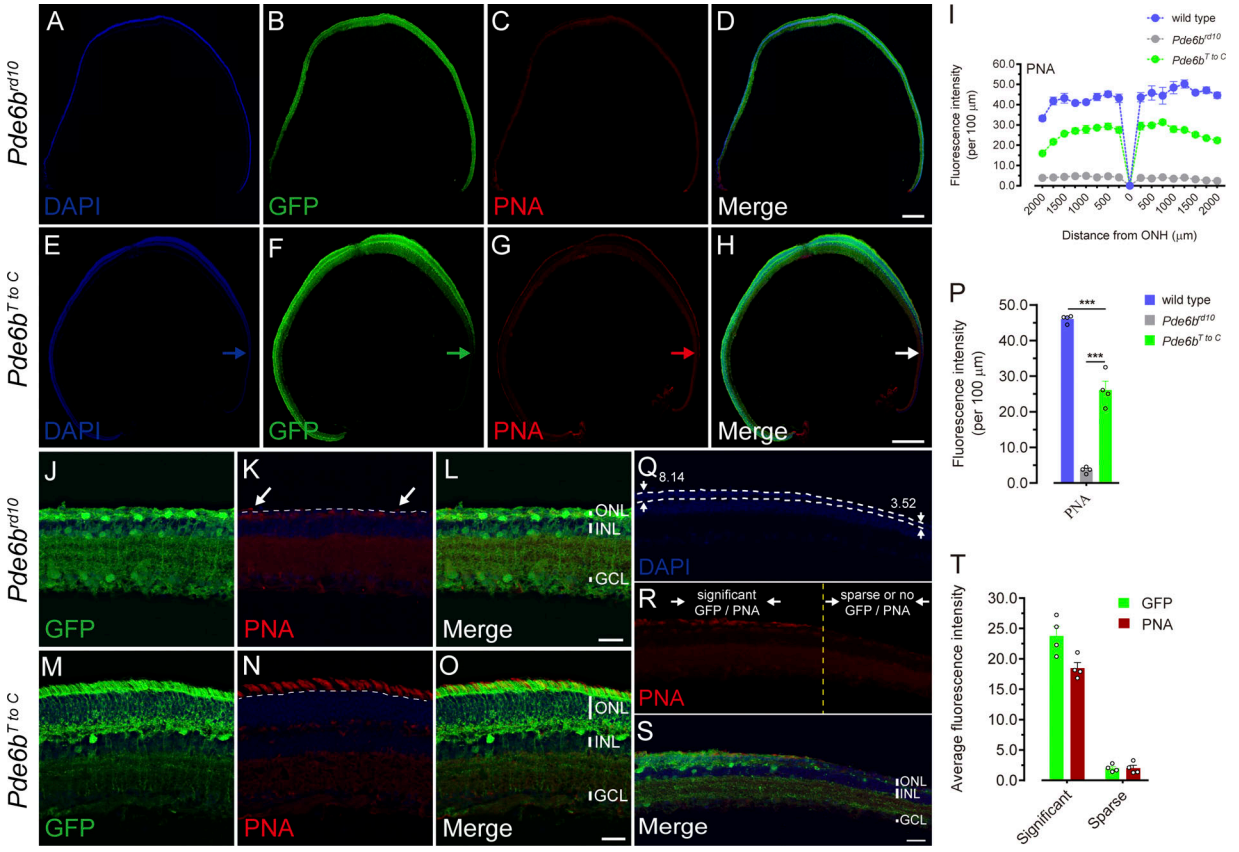

Figure 4. **Cone photoreceptors are significantly preserved in the *Pde6b*^{rd10} mouse retinas treated with PE^{SpRY} system and *gPde6b*. (A–I)** Cone photoreceptor preservation in the *Pde6b*$^{T\ to\ C}$ mice. The retinas from *Pde6b*^{rd10} control mice (A–D) or *Pde6b*$^{T\ to\ C}$ mice (E–H) were sectioned and raised for PNA antibody. Representative images are shown and the fluorescence intensities are quantified in I. Representative data are presented as mean ± SEM; n = 3 independent biological replicates. Blue, DAPI; green, GFP; red, PNA. The arrows in E–H indicate the positions where GFP and PNA signals attenuate concomitantly. Scale bars, 300 μm. **(J–P)** Examination of PNA immunohistochemistry with higher magnification for *Pde6b*^{rd10} control (J–L) and *Pde6b*$^{T\ to\ C}$ (M–O) retinal sections. Arrows in K indicate sparse PNA signals left in the *Pde6b*^{rd10} control retinas. Representative images were shown, and the fluorescence intensities are quantified in P. Representative data are presented as mean ± SEM; n = 4 independent biological replicates. One-way ANOVA tests with Tukey's multiple comparisons. ***, P < 0.001. INL, inner nuclear layer; GCL, ganglion cell layer. Scale bars, 20 μm. **(Q–T)** GFP and PNA signals attenuate steadily and concomitantly in *Pde6b*$^{T\ to\ C}$ mice. Numbers in Q present the thickness of the regions indicated with arrows. The ONL is indicated with white dashed lines. The yellow vertical line in R demonstrates the position where GFP and PNA signals attenuate concomitantly. Representative images are shown and the fluorescence intensities are quantified in T. Representative data are presented as mean ± SEM; n = 4 independent biological replicates. Two-way ANOVA tests with Tukey's multiple comparisons. Scale bars, 20 μm. All of *Pde6b*^{rd10} control retinas were treated with PE^{SpRY} and gScrambled. All experiments were independently performed at least three times to ensure repeatable results.

at P14 (Fig. S3, N–U), suggesting the effective prevention from photoreceptor degeneration elicited by PE^{SpRY}-mediated genome editing in the *Pde6b*^{rd10} mice.

The restoration of compromised PDE enzymic function in the *Pde6b*^{rd10} mouse retinas treated with PE^{SpRY} system and *gPde6b*

The membrane-associated PDE6 plays an indispensable role in initiating rod phototransduction triggered by light stimulation. The catalytic core of functional PDE6 holoenzyme, PDE6β, along with PDE6α facilitates the hydrolysis of cyclic guanosine monophosphate (cGMP) into GMP, leading to the closure of cGMP-gated cation channels, which causes hyperpolarization and hierarchical signal transmission to the neurons housing in the inner nuclear layer. To assess whether the compromised function of PDE6β was restored in the *Pde6b*^{rd10} mice through PE^{SpRY}-elicited genome editing, we measured the PDE activities. In retinal samples from wild-type mice, the PDE activity reached 2.06 ± 0.10 μU/mg at P14 and rose mildly to 2.29 ± 0.03 μU/mg at P120 compared with *Pde6b*^{rd10} control mice treated with PE^{SpRY} and gScrambled, in which PDE activities were as low as 0.24 ± 0.01 and 0.11 ± 0.01 μU/mg at P14 and P120, respectively. Instead, PDE activities in samples from *Pde6b*$^{T\ to\ C}$ mice at P14 were the same as those in *Pde6b*^{rd10} mice, yet rose to 1.81 ± 0.04 μU/mg, suggesting the restoration of PDE activity to a significant extent after genome editing (Fig. 5 A). To examine the genuine involvement of functional PDE6 holoenzyme in hydrolyzing cGMP, we measured the levels of endogenous cGMP in retinas. The samples from wild-type retinas presented a cGMP level as low as 6.51 ± 0.3 nM at P14 and 6.94 ± 0.4 nM at P120, respectively, whereas it reached 10.94 ± 0.3 nM in the *Pde6b*$^{T\ to\ C}$ context at P14. However, the level apparently dropped to 7.20 ± 0.1 nM at P120, providing convincing evidence that the function of PDE6β was substantially restored

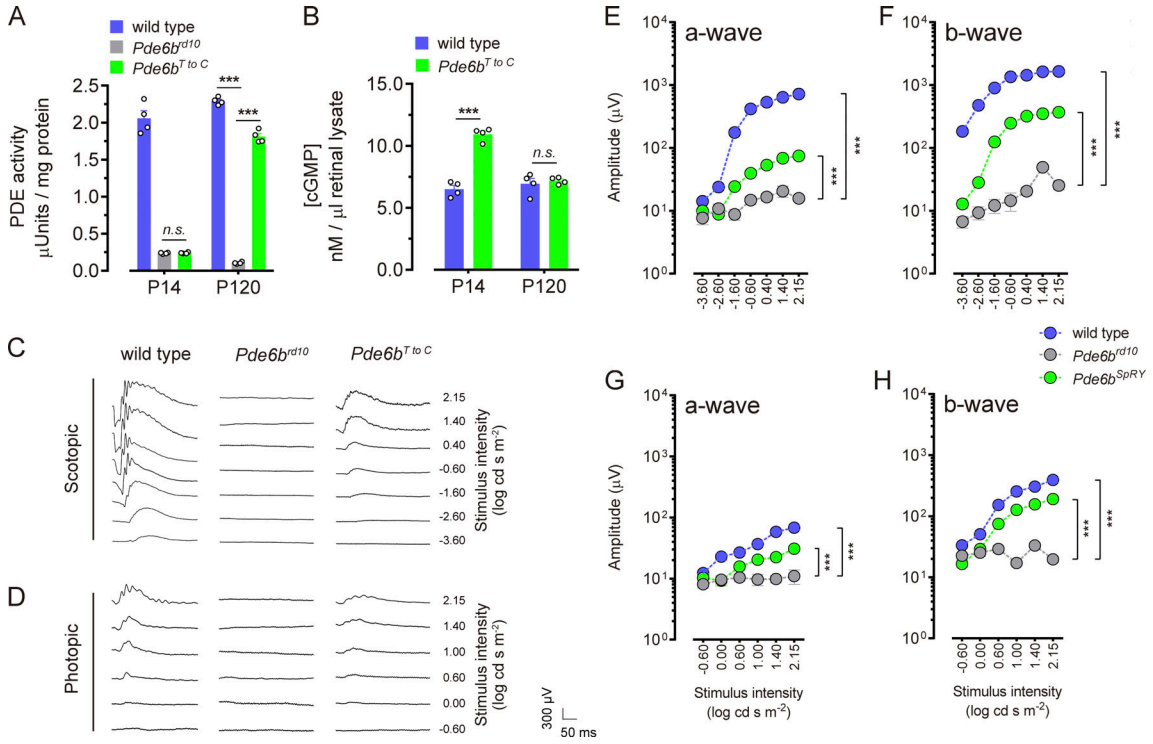

Figure 5. **Restoration of functional PDE6 enzyme and improvement of ERG in the *Pde6b*^{rd10} mice treated with PE^{SpRY} system and *gPde6b*. (A)** PDE activities are restored in the *Pde6b*$^{T\ to\ C}$ mice at P120 to the level comparable to wild-type mice. **(B)** cGMP is hydrolyzed to a considerable extent in the *Pde6b*$^{T\ to\ C}$ mice at P120. Data in A and B are presented as mean ± SEM; *n* = 4 independent biological replicates. Two-way ANOVA tests with Tukey's multiple comparisons. ***, P < 0.001; n.s., P >0.05. **(C–H)** ERG responses are significantly improved in the *Pde6b*$^{T\ to\ C}$ mice. Representative scotopic (C) and photopic (D) ERG responses in the wild-type mice, *Pde6b*^{rd10} control mice, and *Pde6b*$^{T\ to\ C}$ mice at P120. ERGs were recorded in dark-adapted mice (C) with the light intensities increasing from −3.6 to 2.15 log cd s m^{-2} and in light-adapted mice (D) from −0.6 to 2.15 log cd s m^{-2}. The amplitudes of a- (E and G) and b-wave (F and H) were measured for scotopic (E and F) or photopic (G and H) ERG. Data are presented as mean ± SEM; *n* = 6 independent biological replicates. Two-way ANOVA tests with Tukey's multiple comparisons. ***, P < 0.001. All of *Pde6b*^{rd10} control retinas were treated with PE^{SpRY} and gScrambled. All experiments were independently performed at least three times to ensure repeatable results.

with the implementation of genome editing by the PE^{SpRY} system in the retinas of *Pde6b*^{rd10} mice (Fig. 5 B).

Pde6b^{rd10} mice treated with PE^{SpRY} system and *gPde6b* exhibited significantly improved ERG responses

We then sought to assess whether PE^{SpRY}-elicited mutation correction leads to visual improvement via ERG recordings. Scotopic ERGs were recorded in dark-adapted mice with the light intensities increasing from −3.6 to 2.15 log cd s m^{-2}. The rod-dominated responses from wild-type mice showed a steady increase in amplitudes of both a- and b-waves (Fig. 5, C and D). As for the situation in *Pde6b*^{rd10} control contexts treated with PE^{SpRY} and gScrambled, no responses were detected at P120 when nearly all of photoreceptors have lost in ONL. Actually, both scotopic and photopic ERG responses in the *Pde6b*^{rd10} control mice have attenuated to a negligible level since P49 (Fig. S4, A–D). In the age-matched gene-corrected mice, however, the average a- and b-wave amplitudes were 74.6 ± 4.0 and 369.8 ± 8.9 μV for *Pde6b*$^{T\ to\ C}$, and 55.3 ± 7.3 and 285.0 ± 15.1 μV for *Pde6b*^{AGA} mice (Fig. 5, E and F; and Fig. S4, E, G, and H), respectively, as the light intensity achieved 2.15 log cd s m^{-2}, indicating a lesser extent of increase compared to those in wild-type mice. For the photopic ERGs, the light-adapted a-wave in wild-type mice was not evident until the light intensity rose to 0.6 log cd s m^{-2} and reached 68.0 ± 5.4 μV in amplitudes at 2.15 log cd s m^{-2}, while the b-wave had an increase up to 391.6 ± 32.1 μV in amplitudes (Fig. 5, G and H). In line with the situation under the dark adaption, the photopic response was hardly recorded in the PE^{SpRY} and gScrambled-treated *Pde6b*^{rd10} control mice at P120, whereas it was apparently detectable from the eyes subjected to genome editing, with a b-wave amplitude maximally reaching around 191.4 ± 4.8 μV, though only a very minor a-wave was presented (30.8 ± 1.2 μV; Fig. 5, G and H). In addition, the ERG responses were also improved in the *Pde6b*^{AGA} mice (averaging 19.7 ± 2.4 and 154.9 ± 7.3 μV for a- and b-wave, respectively; Fig. S4, F, I, and J), strongly suggesting the apparent ERG responses in the *Pde6b*$^{T\ to\ C}$ and *Pde6b*^{AGA} mice at P120 were indeed a consequence of PE^{SpRY}-elicited mutation correction. For *Pde6b*$^{T\ to\ C}$ mice treated at P21, a significant, though minor, b-wave remained under both scotopic (averaging 50.9 ± 6.5 μV; Fig. S4, K and M) and photopic (averaging 29.1 ± 2.5 μV; Fig. S4, N and P) conditions at 2.15 log cd s m^{-2} despite the insignificantly increased a-wave amplitudes (Fig. S4, K, L, N, and O).

The improved passive and active avoidance in the *Pde6b*^{rd10} mice treated with PE^{SpRY} system and *gPde6b*

To provide substantial evidence that the visual function was indeed improved in the *Pde6b*^{rd10} mice subjected to PE^{SpRY}

JEM

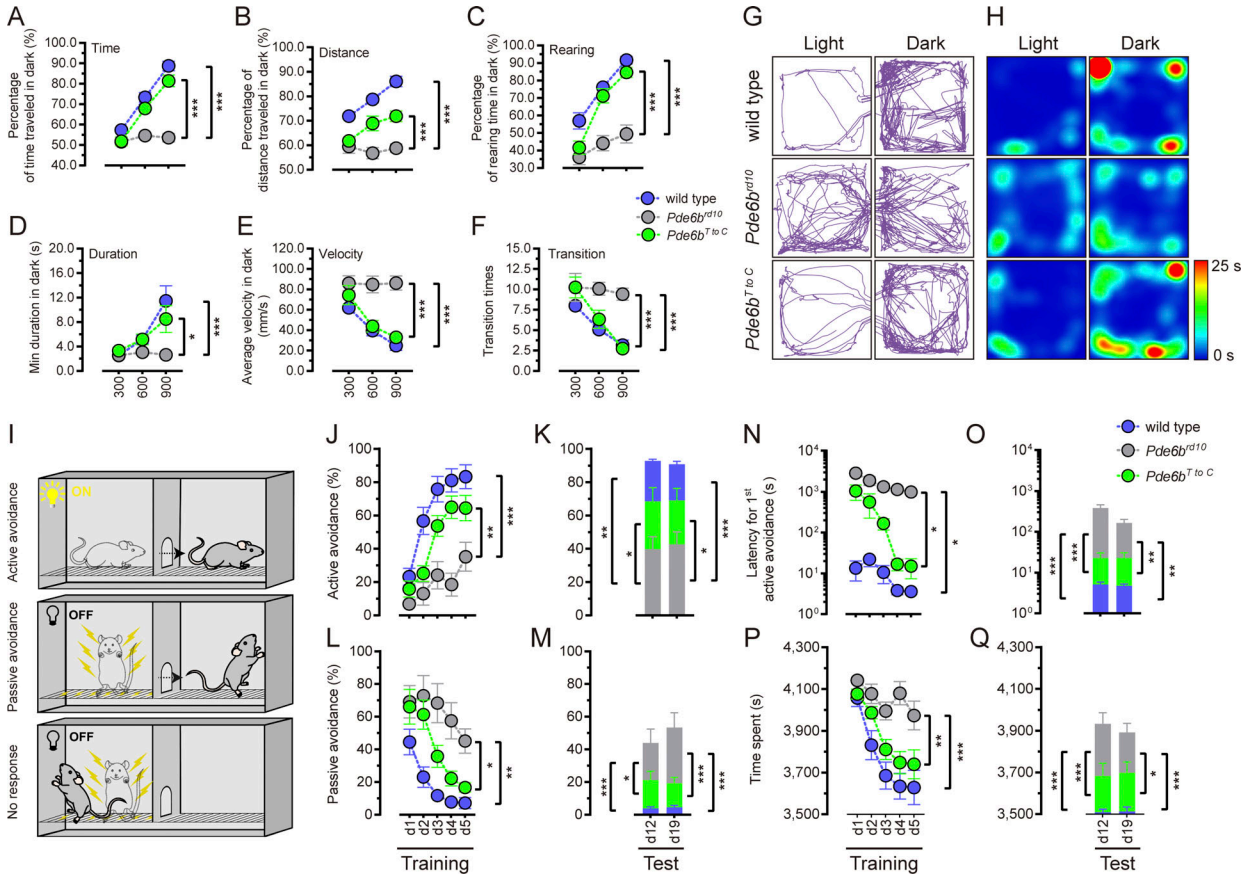

Figure 6. **The improved passive and active avoidance in the *Pde6b*^{rd10} mice treated with PE^{SpRY} system and g*Pde6b*. (A–F)** *Pde6b*$^{T\ to\ C}$ mice exhibit significant improvement of passive avoidance in the light–dark transition test. With the luminance increasing from 300 to 900 lux, the *Pde6b*$^{T\ to\ C}$ mice demonstrate an apparent preference for staying in the dark chamber based on their behavioral parameters including time (A), distance traveled (B), rearing time (C), duration (D), velocity (E) in dark, as well as transition (F) between the chambers. **(G and H)** The representative traveling trajectories (G) and heat map recordings for time spent in distinct regions of the light–dark box (H) with 900 lux luminance. **(I)** Schematic of the shuttle box learning test. **(J–Q)** *Pde6b*$^{T\ to\ C}$ mice demonstrate improved active avoidance both in the 5-d training session (J, L, N, and P) and following test (K, M, O, and Q); the percentage of active avoidance (J and K) and passive avoidance (L and M), latency for the first active avoidance (N and O), as well as time spent (P and Q) in the test were recorded. The mice were 120 d old at d1 of the training session, and 132 and 139 d old (that is, 118 and 125 d after treatment) at d12 and d19 of the test session, respectively. Representative data are presented as mean ± SEM; $n \geq 8$ independent biological replicates. Two-way ANOVA tests with Tukey's multiple comparisons. *, P < 0.05; **, P < 0.01; ***, P < 0.001. All of *Pde6b*^{rd10} control mice were treated with PE^{SpRY} and gScrambled. All experiments were independently performed at least three times to ensure repeatable results.

system-elicited gene correction, we first carried out behavioral assessments for the passive avoidance via the light–dark transition test. With the luminance increasing from 300 to 900 lux, the *Pde6b*$^{T\ to\ C}$ mice demonstrated an apparent preference for staying at the dark chamber over 80% of time (Fig. 6 A), around 70% of distance traveled (Fig. 6 B), and up to 84% of rearing time (Fig. 6 C) in dark, which were a little inferior to those in wild-type mice (averaging 88.8 ± 2.3%, 86.0 ± 2.1%, and 91.3 ± 2.1%, respectively), whereas much better than those in the *Pde6b*^{rd10} mice treated with PE^{SpRY} and gScrambled (averaging 53.6 ± 2.0%, 58.8 ± 1.7%, and 49.5 ± 5.1%, respectively). Meanwhile, the minimal duration in dark significantly kept rising (averaging 3.3 ± 0.5–8.5 ± 2.2 s; Fig. 6 D) whereas the velocity in the dark declined (averaging 74.4 ± 9.4–33.0 ± 3.5 mm/s; Fig. 6 E) with the luminance increasing, which was further confirmed by the reduced transition times from dark to light (averaging 10.2 ± 1.3–2.8 ± 0.4; Fig. 6 F). These performances were very close to those in the wild-type (averaging 11.5 ± 2.5 s, 24.9 ± 4.6 mm/s, and 3.2 ± 0.6 at the luminance of 900 lux) in comparison with the hardly detectable passive avoidance in the *Pde6b*^{rd10} mice treated with PE^{SpRY} and gScrambled (averaging 2.6 ± 0.4 s, 86.2 ± 6.8 mm/s, and 9.4 ± 0.7 at the luminance of 900 lux). The preferred movements in dark were more intuitively presented in traveling trajectories (Fig. 6 G) and the heat maps recording time spent at distinct regions of the light–dark box (Fig. 6 H). On the contrary, the *Pde6b*^{rd10} control mice treated with PE^{SpRY} and gScrambled did not exhibit any apparent preference for the dark chamber, not to mention the comparison with the performance of wild-type mice (Fig. 6, A–H).

In addition, we further examined the active avoidance of these mice via the shuttle box learning test, during which the mice would become much more sensitive to conditioned light due to an electrical shock when they failed to escape (Fig. 6 I). In the 5-d training session, the *Pde6b*$^{T\ to\ C}$ mice showed a stepwise improved active avoidance acquisition with a percentage increase from averaging 15.8 ± 4.9% on the first day to 64.5 ± 7.6%

at the end of the training (the fifth day; Fig. 6 J), corresponding to a decline of passive avoidance from averaging 66.0 ± 10.6 to 16.7 ± 2.8% (Fig. 6 L), which was nearly to keep up with their age-matched wild-type mouse performance. By contrast, the *Pde6b*^{rd10} control mice treated with PE^{SpRY} and gScrambled exhibited rather poor active avoidance performance with an average level of no more than 40% (35.2 ± 8.7%; Fig. 6 J) and up to 45.1 ± 7.4% passive avoidance (Fig. 6 L) and appeared unresponsive in the remaining around 20% of trials, suggesting the difficulty in acquiring correlation between the light and the electrical shock in these mice due to their poor vision. As for the latency, the time to the first active avoidance decreased steadily from around 1,000 to 15.1 ± 7.7 s on the fifth day for the *Pde6b*$^{T\ to\ C}$ mice, which was close to the performance of wild-type ones (3.6 ± 0.6 s; Fig. 6 N), suggesting they have good knowledge of the setup, despite a relatively mild change in the *Pde6b*^{rd10} control treated with PE^{SpRY} and gScrambled. As expected, the time traveled during the training decreased steadily and significantly both in the *Pde6b*$^{T\ to\ C}$ and in the wild-type mice, irrespective of the struggling and somewhat irregular change in the *Pde6b*^{rd10} control treated with PE^{SpRY} and gScrambled (Fig. 6 P). We then moved forward to test the animal responses 1 and 2 wk after the end of training (d12 and d19), and the performance in the *Pde6b*$^{T\ to\ C}$ mice and in the wild-type ones remained relatively stable or became even better than that in the training session while no substantial changes were detected in the *Pde6b*^{rd10} control treated with PE^{SpRY} and gScrambled (Fig. 6, K, M, O, and Q).

Pde6b^{rd10} mice treated with PE^{SpRY} system and g*Pde6b* demonstrated apparent visually driven optomotor responses

It is generally conceivable that mice would appear responsive to different spatial frequencies and contrasts once the vision is functionally restored to a certain degree. To quantitatively determine how much the vision was improved in PE^{SpRY} system–treated mice, we sought to evaluate the visual function by an automated system with optomotor responses accurately and objectively recorded through video tracking algorithms (Fig. 7, A and B; Kretschmer et al., 2015). Both left and right eyes of wild-type mice exhibited approximately equal contributions to the total optomotor responses elicited by a panel of stimulus at defined spatial frequencies (0.02, 0.1, 0.15, 0.2, 0.3, and 0.4 cycles/°) or contrasts (100, 50, 25, 12.5, 10, and 5%; Fig. 7, C and D), suggesting a reliable and unbiased detection by the system.

To globally assess the visually driven optomotor responses, the ratios of response time between the head movements in the correct and incorrect directions, namely OMR (optomotor reflex), were assayed in terms of a wide range of velocity thresholds at defined spatial frequency or contrast levels (Fig. 7, E and F). It is anticipated that the overall OMR values in wild-type context appeared relatively higher at a spatial frequency of 0.02 cycles/°, culminating at 0.2 cycles/° as OMR exhibited equal to or higher than 2.0 (presented in red) in most velocity thresholds (Fig. 7 E), followed by a decline afterward and drop to a nearly undetectable level at 0.4 cycles/°. By contrast, visual stimuli–driven responses in the *Pde6b*^{rd10} degenerative context treated with PE^{SpRY} and gScrambled sustained a barely detectable level at all spatial frequencies tested as OMR values were no higher than 1.2 within most thresholds (in blue). Regardless of a relatively lower OMR at the beginning, the visual stimuli–driven response exhibited an obvious increase at a spatial frequency of 0.2 cycles/° in the *Pde6b*$^{T\ to\ C}$ mice and then declined steadily to an inappreciable level, essentially in line with the trend in wild-type context. As for the contrasts, the visual stimuli–driven response in the *Pde6b*$^{T\ to\ C}$ mice started with the highest level at 100% contrast and tapered down gradually from 50 to 5%, showing a parallel change with the situation in the wild-type mice (Fig. 7 F).

The head movement unrelated to visual stimuli is likely to be minimized when the ideal velocity threshold criteria are set and the range between 2 and 14°/s is regularly recommended based on previous observation (Kretschmer et al., 2015). We thus carried out an investigation on the comparison of visual stimuli–driven responses under these optimal velocity conditions (the boxed ranges colored in magenta and green; Fig. 7, G and H; and Fig. S5, A–D). For an intuitive and uniform evaluation of data acquired at different conditions, the response time in either direction (correct or incorrect) at each velocity interval (1°/s in each interval) was normalized to the maximal response time (designated as 1) under each spatial frequency or contrast tested. Compared with those in the opposite direction (negative value, light magenta window), the occurrence of visually driven optomotor responses at 0.2 cycles/° in the *Pde6b*$^{T\ to\ C}$ mice was apparently more frequent and lasted longer (blue bars) in the stimulus direction (positive value, light green window), and the OMR value at 0.2 cycles/° was therefore up to 2.15. Accordingly, OMR values at 0.02, 0.3, and 0.4 cycles/° were 1.66, 1.45, and 1.08, respectively (Fig. 7 G). For the contrasts tested, OMR values appeared maximal at 100% contrast and were equal to 2.09, with a steady decline when the contrast levels were decreasing (Fig. 7 H). Combined with the observations at different spatial frequencies, the trends of OMR values were essentially consistent with the profiles of the heat maps presented in Fig. 7, E and F, with a particular emphasis on the parallel changes of visual responses between *Pde6b*$^{T\ to\ C}$ and wild-type (Fig. S5, A and B) rather than *Pde6b*^{rd10} degenerative control mice treated with PE^{SpRY} and gScrambled (Fig. S5, C and D).

Since the difference between $T_{correct}$ (total time animal head moved in the stimulus direction) and $T_{incorrect}$ (total time animal head moved in the opposite direction) in totally blind mice were theoretically close or equal to 0, we, therefore, assessed the visual function with $T_{correct} - T_{incorrect}$, hereafter named as ΔT, for a much more obviously intuitive method to measure the visual stimuli–driven responses. As expected, in the *Pde6b*^{rd10} degenerative context treated with PE^{SpRY} and gScrambled, the optomotor responses were barely detectable at a panel of spatial frequencies and contrast tested (Fig. 7, I and J). By contrast, the responses showed parallel changes in the *Pde6b*$^{T\ to\ C}$ mice with those in the wild-type context, with a maximal response at a spatial frequency of 0.2 cycles/° and 100% contrast, respectively. Together, the enhanced optomotor responses suggested an improved visual function in the PE^{SpRY} system–treated mice.

The optomotor responses demonstrated above were essentially contributed by both eyes of each mouse; the conclusion,

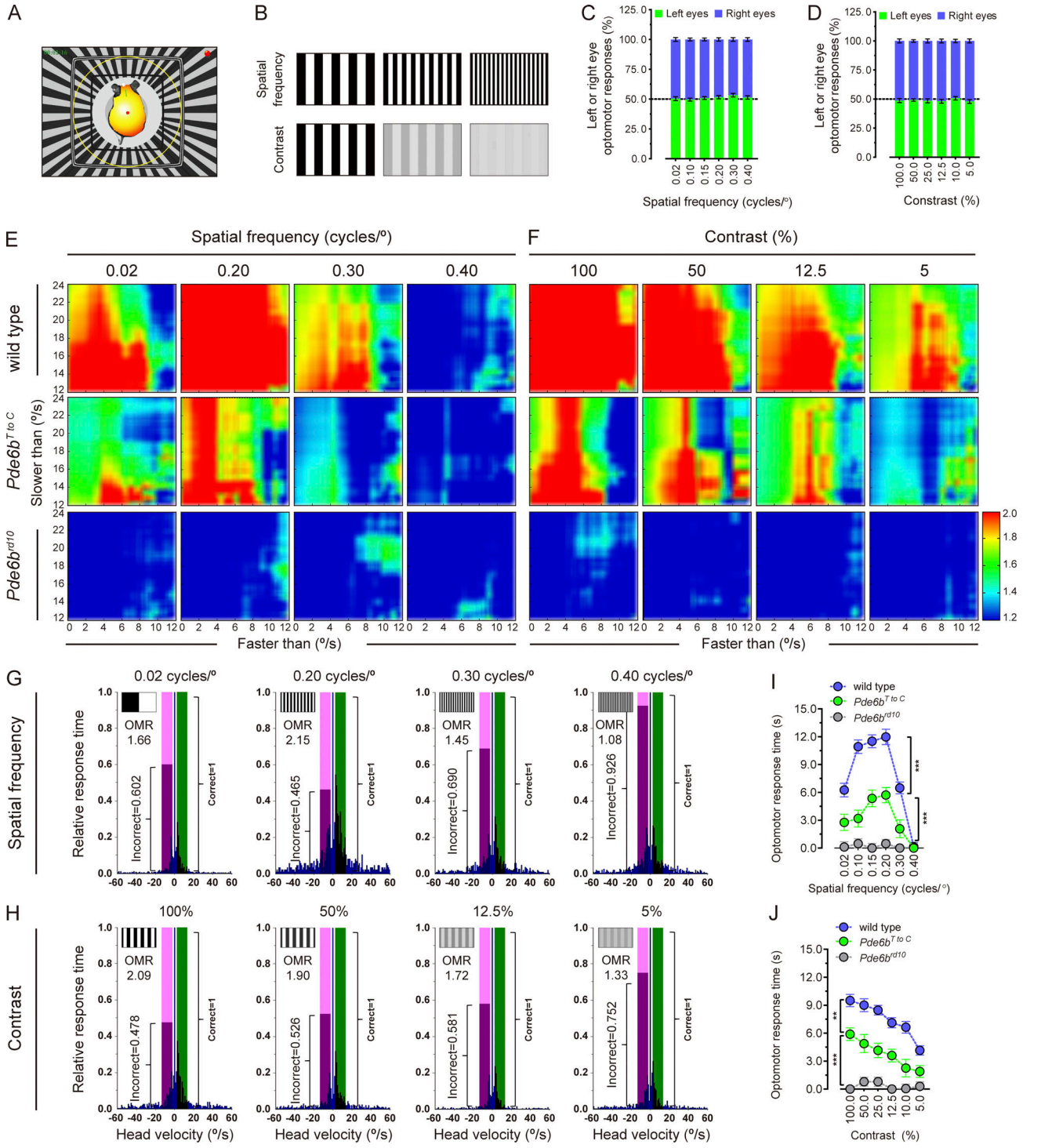

Figure 7. **Visual rescue determined by visually driven optomotor behavior test in the *Pde6b*^{rd10} mice treated with PE^{SpRY} system and g*Pde6b*. (A)** The automated optomotor system setup. **(B)** Visual function is evaluated through a series of stimuli at defined spatial frequencies and contrasts. **(C and D)** The equal contribution of both left and right eyes in the wild-type mice to the optomotor responses at defined spatial frequencies (C) or contrasts (D). Representative results were shown, and data are presented as mean ± SEM. **(E and F)** The visual stimuli–driven optomotor responses are globally significant in the *Pde6b*$^{T\ to\ C}$ context when tested at defined spatial frequencies (E) or contrasts (F). Representative heat maps indicate OMR values at a wide range of velocity thresholds at defined spatial frequency or contrast levels. **(G and H)** The visual stimuli–driven optomotor responses are significant in the *Pde6b*$^{T\ to\ C}$ context when tested at defined spatial frequencies (G) or contrasts (H) under the optimal velocity conditions (2–14°/s). The response time in either stimulus direction (positive value, light green window) or opposite direction (negative value, light magenta window) at defined velocity thresholds is normalized to the maximal response time, which is herein defined as 1 and presented as a blue bar. The OMR values at each spatial frequency or contrast are indicated with a magenta bar normalized to green one defined as 1 if the response time in the stimulus direction is longer than that in the opposite direction, and vice versa. Here, the heights of green bars are the same as those of light green bars when the response time in the stimulus direction is longer than that in the opposite direction, so the light green bars are covered by green bars. Representative results were shown. **(I and J)** The difference between the head moving time in the stimulus direction and

that in the opposite direction, namely ΔT, in the *Pde6b*$^{T\ to\ C}$ context intuitively shows a parallel change with the situation in the wild-type mice when tested at defined spatial frequencies (I) or contrasts (J) under the optimal velocity conditions (2–14°/s). Representative data are presented as mean ± SEM; $n \geq 8$ independent biological replicates. Two-way ANOVA tests with Tukey's multiple comparisons. **, P < 0.01; ***, P < 0.001. All of *Pde6b*^{rd10} control mice were treated with PE^{SpRY} and gScrambled. All experiments were independently performed at least three times to ensure repeatable results.

however, would be generally more convincing if a comparison between paired contralateral eyes yet treated with different vectors is performed. With the aim to address this issue, we only treated one eye with PE^{SpRY} and g*Pde6b*$^{T\ to\ C}$, leaving the contralateral one treated with control vectors, and evaluated the optomotor response levels at the optimal condition with 0.2 cycles/° spatial frequency and 100% contrast. The global OMR profiles appeared comparable in both the left and right eye of the wild-type mouse (Fig. 8 A, top panel). It is intriguing, however, that the visual stimuli–driven responses in the clockwise direction appeared much more evident than those in the counterclockwise direction when the left eye was treated with PE^{SpRY} and g*Pde6b*$^{T\ to\ C}$, whereas the right one with PE^{SpRY} and gScrambled, and vice versa (Fig. 8 A, middle and bottom panels). As for the test under the optimized velocity threshold (2–14°/s), the OMR values for the left and right eyes from wild-type context were 2.81 and 2.76, respectively, suggesting the comparable and evident visual function for both eyes. In the degenerative context, the left eye treated with PE^{SpRY} and g*Pde6b*$^{T\ to\ C}$ had an OMR value equal to 2.06 versus 1.07, a clear "blindness" indicator, in the right one treated with PE^{SpRY} and gScrambled, which was the case when the visual improvement was occurring exclusively in the right eye (Fig. 8 B). The evaluation of visual stimuli–driven responses based on the ΔT was becoming more conclusive with a value of as low as 0 for internal control eyes compared with the obvious visual activities recorded from their contralateral eyes (Fig. 8 C). These observations were substantially evidenced by the immunohistochemical assays, in which the rod photoreceptors were only preserved in retinas transduced with PE^{SpRY} and g*Pde6b*$^{T\ to\ C}$ vectors, in striking contrast to the situation in those transduced with control vectors (Fig. 8 D). In addition, we sought to evaluate whether the visual function could be well sustained in the aged mice after PE^{SpRY} system treatment. Compared with the complete loss of visually driven optomotor responses in age-matched *Pde6b*^{rd10} control mice treated with PE^{SpRY} and gScrambled, the visual function in the *Pde6b*$^{T\ to\ C}$ mice remained relatively stable throughout the ages tested (from P150 to P240; Fig. 8 E), with average ΔT values of no less than 5 s at the 0.2 cycles/° spatial frequency and 100% contrast (Fig. 8 F), further suggesting the efficiency and persistence of photoreceptor rescue via PE^{SpRY} system–elicited in vivo genome editing.

Pde6b^{rd10} mice treated with PE^{SpRY} system and g*Pde6b* solved the visually guided water task

Finally, we assessed visual capabilities using the discrimination task, a visually guided water-maze test, which requires cognitive processing of visual information to associate a grating with a submerged hidden platform allowing them to escape from the water in a trapezoidal-shaped tank (Fig. 9 A; Prusky et al., 2000). During the 4-d (D1–D4) training period with four sessions (S1–S4) per day (Fig. 9, B–D), the *Pde6b*^{rd10} control mice treated with PE^{SpRY} and gScrambled were rarely able to correctly complete the task in at least 70% of trials (Fig. 9 C) compared with wild-type mice, who performed better than 70% of chance since the second day and responded correctly in up to averaging 97.5 ± 2.5% of trials at the last session of D4 (D4S4; Fig. 9 B). In contrast to their aging-matched counterparts, *Pde6b*$^{T\ to\ C}$ mice gave rise to a much better performance with a correct choice steadily rising to 70% (72.5 ± 2.5%) at S1 of D2 and reaching ∼90% (87.5 ± 2.5%) by the end of training (Fig. 9 D). Their traveling trajectories during training sessions were correspondingly presented in an orderly manner (Fig. 9 F), which was close to those of wild-type mice (Fig. S5 E), as further evidenced in the heat maps indicating the group-average time traveled at defined positions (Fig. S5, F and H). In comparison, the *Pde6b*^{rd10} control mice treated with PE^{SpRY} and gScrambled appeared to struggle to localize the platform throughout the training (Fig. 9 E and Fig. S5 G).

When tested for the visual acuity and contrast sensitivity, both *Pde6b*$^{T\ to\ C}$ and wild-type mice performed best at 0.2 cycles/° spatial frequency or at 100% contrast and demonstrated a clear and visually guided response with the change of conditions tested. In particular, the *Pde6b*$^{T\ to\ C}$ mice were capable of solving the cognitive task when the spatial frequency was as high as around 0.4 cycles/°, which was comparable to the visual acuity shown in wild-type mice (Fig. 9 G). This was also the case when the mice were tested at steadily declined contrasts (Fig. 9 H). The *Pde6b*$^{T\ to\ C}$ mice were able to pass the test once the contrast was over 25%, which was only a little inferior to the contrast sensitivity indicated in the wild-type mice, not to mention the failure in completing the task at all spatial frequencies and contrast levels tested in the *Pde6b*^{rd10} control mice. The performance of *Pde6b*$^{T\ to\ C}$ and wild-type mice was confirmed by their minimal latency time and distance traveled at 0.2 cycles/° spatial frequency (Fig. 9 J and Fig. S5 I) and 100% contrast (Fig. 9 L and Fig. S5 J), respectively. In contrast, the *Pde6b*^{rd10} control mice treated with PE^{SpRY} and gScrambled performed so poorly that their latency time spent in finding the platform was much longer than that of *Pde6b*$^{T\ to\ C}$ and wild-type mice and exhibited irregular profiles as far as both the time and distance traveled were concerned (Fig. 9, I and K). These observations were consistent with the contexts of the heat maps reflecting the group-average time traveled at defined positions as well (Fig. 9 M and Fig. S5 K). For each of the mice tested in the water maze, both *Pde6b*$^{T\ to\ C}$ and wild-type groups completed the task with a correct rate over 70% compared with the complete failure of all *Pde6b*^{rd10} control mice treated with PE^{SpRY} and gScrambled (Fig. 9 N). In addition, the test in the *Pde6b*^{AGA} mice further supported the efficient genome editing elicited by the PE^{SpRY} system (Fig. S5, L–P).

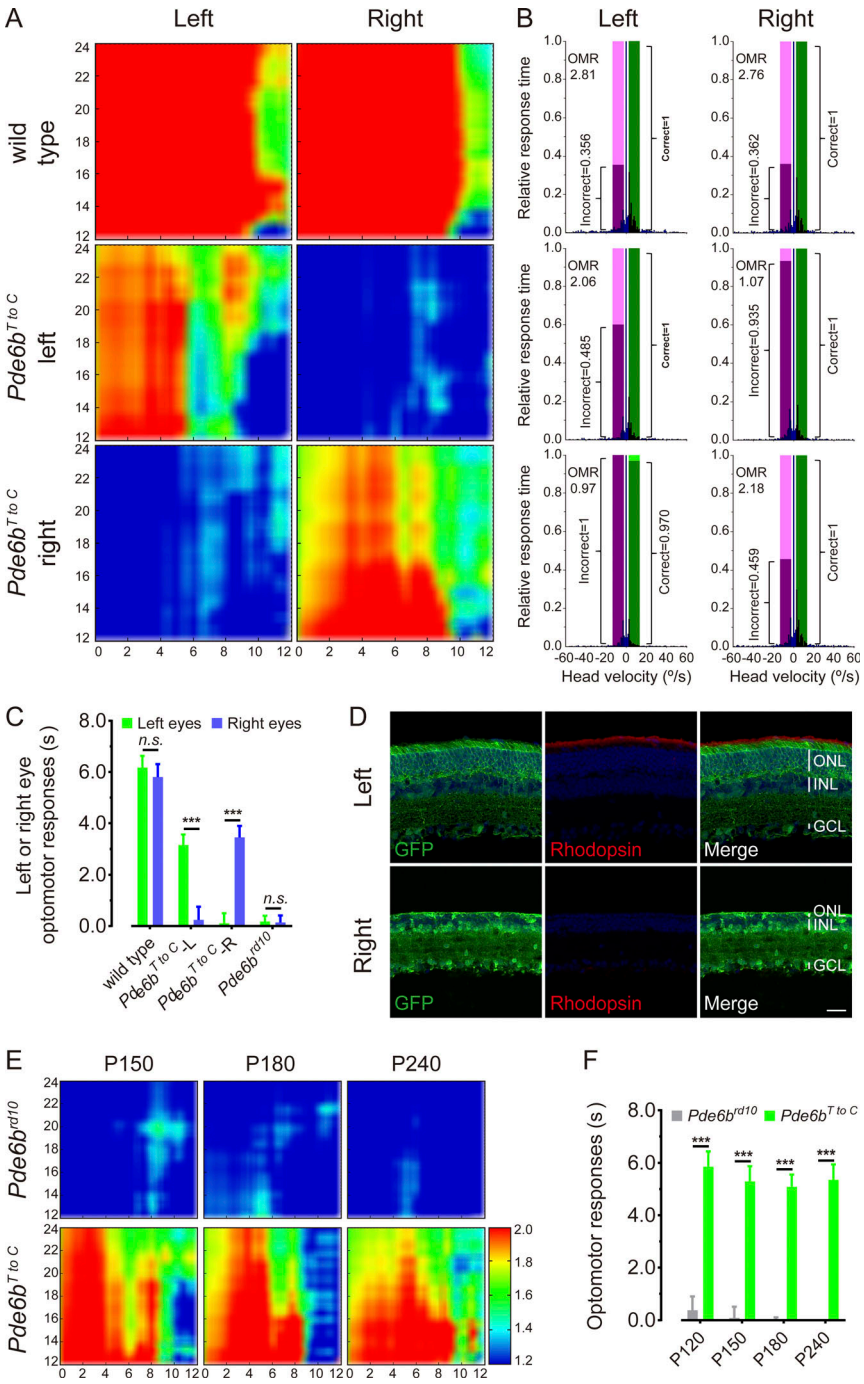

Figure 8. **The impaired vision is restored in the individual eyes and in aged *Pde6b*^{rd10} mice treated with PE^{SpRY} system and g*Pde6b*. (A)** The visual stimuli–driven optomotor responses are globally significant in the individual eyes treated with PE^{SpRY} and g*Pde6b*$^{T\ to\ C}$ when tested at the optimal condition with 0.2 cycles/° of spatial frequency and 100% of contrast. Representative heat maps indicate OMR values at a wide range of velocity thresholds at defined spatial frequency or contrast levels. **(B)** The visual stimuli–driven optomotor responses are significant in the individual eyes treated with PE^{SpRY} and g*Pde6b*$^{T\ to\ C}$ when tested at the optimal condition with 0.2 cycles/° of spatial frequency and 100% of contrast under the velocity threshold of 2–14°/s. **(C)** The difference between the head moving time in the stimulus direction and that in the opposite direction elicited through the individual eyes in each context under the optimal conditions (0.2 cycles/° spatial frequency, 100% contrast, 2–14°/s velocity threshold). L or R, left or right eye treated with PE^{SpRY} and g*Pde6b*$^{T\ to\ C}$. Representative data are presented as mean ± SEM; $n \geq 8$ independent biological replicates. Two-way ANOVA tests with Tukey's multiple comparisons. ***, $P < 0.001$; n.s., $P > 0.05$. **(D)** Immunohistochemistry for Rhodopsin on the sectioned retinas from mice with left eyes treated with PE^{SpRY} and g*Pde6b*$^{T\ to\ C}$ vectors. Representative images are shown here. INL, inner nuclear layer; GCL, ganglion cell layer. Scale bars, 20 µm. **(E)** Representative heat maps from the visual stimuli–driven optomotor responses in aged mice. **(F)** The difference between the head moving time in the stimulus direction and that in the opposite direction in aged mice. Representative data in F are presented as mean ± SEM; $n \geq 8$ independent biological replicates. Two-way ANOVA tests with Tukey's multiple comparisons. ***, $P < 0.001$. All of *Pde6b*^{rd10} control mice were treated with PE^{SpRY} and gScrambled. All experiments were independently performed at least three times to ensure repeatable results.

Discussion

To date, the applicability and effectiveness of CRISPR-based genome-editing tools have been increased and optimized progressively, driving major advances in nearly every aspect related to gene therapy. As the representatives for this technology, BEs and PEs hold great promise for both basic research and therapeutic applications. The IRDs, for example, have been widely considered an ideal target for CRISPR-based gene therapy (Anzalone et al., 2020; Choi et al., 2022; Jang et al., 2021; Jo et al., 2019; Maeder et al., 2019; Suh et al., 2021; Yu et al., 2017). However, it is worth further consideration for the limitations of utilizing BEs and PEs to implement in vivo genome editing for vision rescue in those studies.

The target cells where genome editing is carried out in those reports are mainly restricted to RPE cells which are non-neuronal cells (Choi et al., 2022; Jang et al., 2021; Suh et al., 2021), and the *Rpe65* gene encodes an isomerase in the visual cycle that regenerates the active visual chromophore 11-cis-retinal in RPE cells (Redmond et al., 1998). Most of the mutations causing RP and other IRDs are instead associated with neural photoreceptor functions and survival (Daiger et al., 2013; Gagliardi et al., 2019). Thus, given the complexity of neural architecture, the direct utility of genome editing in the neural retinal cells, in

JEM

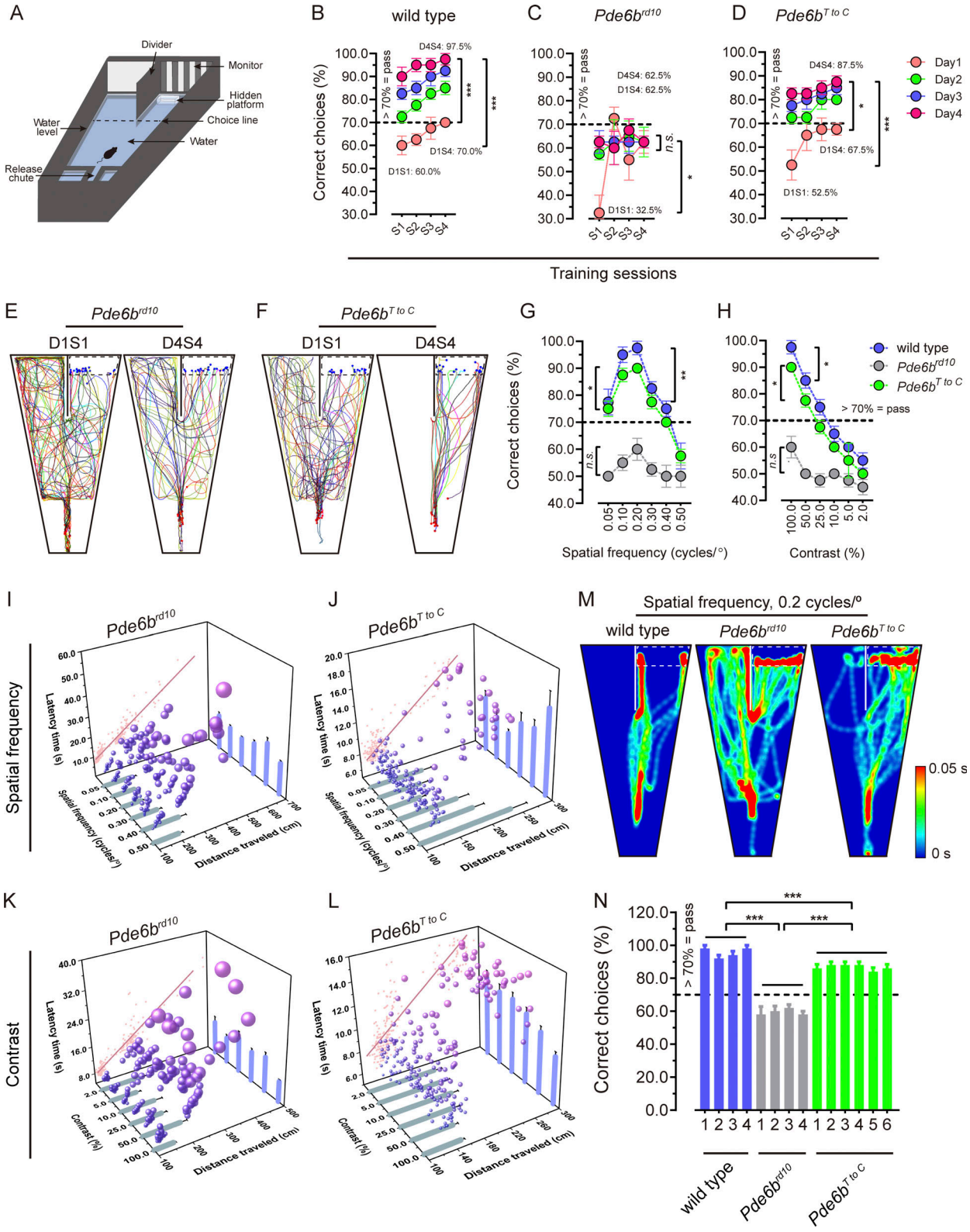

Figure 9. **The *Pde6b*^{rd10} mice treated with PE^{SpRY} system and g*Pde6b* can solve the visually guided water task. (A)** Schematic of the visual water task. **(B–D)** Pass rates of wild-type (B), *Pde6b*^{rd10} control mice (C), and *Pde6b*$^{T\ to\ C}$ mice (D) during the training period for four consecutive days (D1–D4) with four sessions (S1–S4) each day. D1S1, D1S4, and D4S4 mean session 1 of day 1, session 4 of day 1, and session 4 of day 4, respectively. **(E and F)** Representative traveling trajectories of *Pde6b*^{rd10} (E) and *Pde6b*$^{T\ to\ C}$ (F) mice during D1S1 and D4S4. Only trajectories or heat maps for trials with platform placed on the right are shown unless stated otherwise. **(G and H)** Average pass rates of wild-type (blue), *Pde6b*^{rd10} (gray), and *Pde6b*$^{T\ to\ C}$ (green) mice at different spatial frequencies (G) or contrasts (H). **(I–L)** Average swim latency time (cyan bars) and distance traveled (blue bars) of *Pde6b*^{rd10} (I and K) and *Pde6b*$^{T\ to\ C}$ (J and L) mice at different spatial frequencies (I and J) or contrasts (K and L). The coordinates of spheres are determined by latency time, distance traveled, and spatial frequency

or contrast in each test. The sphere sizes indicate the amounts of latency time spent and the pink points are determined by latency time and distance traveled in each test. **(M)** Representative heat map for the group-average of time traveled at distinct positions by wild-type, *Pde6b*^{rd10}, and *Pde6b*$^{T\ to\ C}$ mice under 0.2 cycles/° of spatial frequency. **(N)** Performance of each mouse tested in the water task. Representative data are presented as mean ± SEM, two-way ANOVA followed by Tukey's multiple comparisons test, $n \geq 4$ independent biological replicates. *, P < 0.05; **, P < 0.01; ***, P < 0.001; n.s., P > 0.05. All of *Pde6b*^{rd10} control mice were treated with PE^{SpRY} and gScrambled. All experiments were independently performed at least three times to ensure repeatable results.

particular for unhealthy or dying photoreceptors, would provide much more convincing evidence for the potential applications of these tools in RP treatment. Some studies reported the successful introduction of BEs or PEs into the wild-type retinas for targeted genome editing (Chen et al., 2020; Zhi et al., 2022), which raises further concerns about the effectiveness of genome editing in the retina under the pathological condition. For example, photoreceptor cell death starts as early as P16 in *Pde6b*^{rd10} mice, and only a single row of cell bodies is left in most regions of ONL at no later than P60. Whether the correction via genome editing enables photoreceptor preservation before all of them die or whether the photoreceptors preserved via genome editing are sustained well enough for the rescue of visual function would be totally different from the issue addressed under normal physiological conditions. Our results clearly indicate that PE^{SpRY}-elicited *Pde6b* gene correction is capable of promoting substantial photoreceptor survival in *Pde6b*^{rd10} mice and the visual function preserved exhibits comparable or a little inferior to that in wild-type mice. To our knowledge, the present study is the first report systematically exploiting PE-based strategy to implement gene therapy in the RP disease model. In particular, the visual function is found to be sustained well in the treated *Pde6b*^{rd10} mice as old as P240, which further supports PE^{SpRY} as a reliable genome-editing tool in treating RP.

Another point drawing our attention is the limitation of BEs used for the treatment of inherited retinal diseases. As we know, BEs only enable the installation of point mutations in the genome (Gaudelli et al., 2017; Koblan et al., 2021; Komor et al., 2016), and the bystander edits caused by the presence of the multiple C or A within the editing window have to be carefully considered. As expected, the ABE results in limited precision and unintended bystander edits when used in the correction of point mutation at the *Rpe65* locus (Suh et al., 2021). To address this issue, PEs are used in the same LCA mouse model and produce an efficient single nucleotide substitution without any detectable indels and bystander effects (Jang et al., 2021). Based on these results, however, two critical issues are worth further consideration. One is whether PEs are able to appear versatile enough for in vivo genome editing when the combination edits are desired or when the inherited disorders are caused by mutations in two or more base pairs or in an even more complicated way. In other words, we expect that PEs exhibit versatility as they are doing in the cell lines (Anzalone et al., 2019) and that they are not restricted by editing types when used for the treatment of retinal diseases resulting from multiple mutations. The other is that all editors used in the above-mentioned studies are SpCas9-based proteins. The stringent PAM requirement would generate significant target sequence restrictions, presumably leading to the low efficiency of genome editing and the limited use of this tool. As demonstrated in the present study, the PE^{SpCas9} is incapable of installing desired edits at *Pde6b* locus likely due to its PAM preferences, as the selected canonical PAMs and corresponding protospacers either exhibit lower editing efficiency based on the prediction and experimental tests or are far away from the targeted position, resulting in incompatible long-distance RT templates. To provide a solution for these questions, we use PE^{SpRY}, combining the advantages of PEs and the PAM-less SpRY variant, to successfully and efficiently introduce combination edits such as *Pde6b*^{AGA} into the diseased retinas of *Pde6b*^{rd10} mice and facilitate substantial rescues of both photoreceptors and visual function as well. Of particular importance, all of the 14 PAMs and their protospacers tested appear active, though with differential compatibility, for PE^{SpRY}. Among these PAMs, only one (TGG, corresponding to protospacer p7) displays canonical NGG sequence, but the editing efficiencies with other non-NGG PAMs such as GTG, TGC, and CAG (corresponding to protospacer p5, p4, and p9, respectively) appear much higher, suggesting the relaxed or unconstrained PAM requirement for PE^{SpRY}. In particular, PE^{SpRY} system with GTG as its PAM makes in vivo genome editing for RP mouse model become a reality, which would offer an opportunity for this genome-editing tool for more extensive applications in treating diverse IRDs.

The next point we should pay attention to is the appropriate assessment of the visual function after the correction of mutation causing eye diseases. As generally accepted, whether vision is improved after genome editing or any type of gene therapy relies on detailed behavioral tests. In comparison with previous reports, in which the behaviors were relatively roughly demonstrated after the correction of point mutation via ABEs or PEs in *Rpe65*-associated LCA mouse model (Jang et al., 2021; Suh et al., 2021), we herein carry out a careful behavioral characterization via a light–dark transition test for passive avoidance, shuttle box learning test for active avoidance, and visually guided optomotor response test, as well as water-maze visual discrimination tasks in *Pde6b*^{rd10} mice subjected to PE^{SpRY}-elicited genome editing. The fully automated recordings and assays for each detail of mouse movements guarantee accurate quantitative assessments for the improved visual function, therefore providing solid evidence for the effects of PE^{SpRY} system on the treatment in *Pde6b*-associated RP mouse model. Despite the more objective evaluation of human vision through well-developed instruments such as Goldmann perimetry, microperimetry, and pupillometry, the introduction of multiluminance mobility testing in the phase 3 trial of Luxturna for the treatment of RPE65-associated LCA (Russell et al., 2017), suggesting the indispensability of intuitively evaluating the visual preservation and restoration via behavioral performance. Thus, the demonstration of functional rescue of vision via genome editing in the

Pde6b^{rd10} mice in these real-world simulations provides more conclusive information regarding the preservation of the vision-mediated direction, localization, and motion, and even cognition compared with the histological assay and ERG test.

It is worth noting that non-viral vectors including virus-like particles and lipid nanoparticles are currently emerging as an alternative approach to deliver cargos into the tissues and have demonstrated great potential in treating diseases (Banskota et al., 2022; Raguram et al., 2022). One of the limitations, however, is the size of the non-viral vectors. Typically, the size of AAV is around 20–30 nm whereas those of non-viral vectors generally exceed 100 nm, which precludes the delivery of cargos (DNAs, RNAs, or proteins) into the photoreceptors due to the physical barriers in the eye (such as the outer limiting membranes and the inter-photoreceptor matrix; Trapani et al., 2014). Thus, the non-viral vectors remain to be optimized for their efficiency in transducing neural retinas.

Taken together, we exploited a versatile and unconstrained genome-editing tool, PE^{SpRY}, integrating the advantages of prime editors and SpRY to successfully install desired edits into diseased *Pde6b*^{rd10} mouse retinas. In addition to the significant preservation of both rod and cone photoreceptors and restoration of compromised PDE6 phosphodiesterase activity, the treated mice showed the apparent responses elicited in the ERG test and good performance in a variety of behavioral assessments including passive and active avoidance, optomotor test, as well as water-maze task. By PE^{SpRY}-elicited in vivo correction of mutation at *Pde6b* locus, we ultimately rescued the vision in the *Pde6b*-associated RP mouse model. We provide substantial evidence for the in vivo applicability of this new genome-editing strategy and would further facilitate the realization of its full potential in diverse research and therapeutic contexts, in particular for IRDs.

Materials and methods

Animals

C57BL/6J and *Pde6b*^{rd10} mice were originally purchased from The Jackson Laboratory and bred under controlled ambient illumination on a 12-h/12-h light–dark cycle. All animal procedures were approved by the Wuhan University of Science and Technology ethics committee and performed according to the Institutional Animal Care and Use Committee standards and National Institutes of Health guidelines for the Care and Use of Laboratory Animals.

Plasmid construction

The constructs of pAAV-EF1α-NpuC-SpRY(H840A)$^{714\text{-}1368}$-M-MLV and pAAV-EF1α-GFP-P2A-SpRY(H840A)$^{1\text{-}713}$-NpuN were originally generated from pCMV-PE2 (plasmid 132775; Addgene) and pAAV-EF1α-GFP. In brief, the site mutations (A61R, L111R, D1135L, S1136W, G1218K, E1219Q, N1317R, A1322R, R1333P, R1335Q, and T1337R) were sequentially introduced into the SpCas9 (H840A)-M-MLV (that is, PE^{SpCas9}) through PCR to obtain pCMV-PE^{SpRY}. The three fragments, P2A, SpRY(H840A)$^{1\text{-}713}$ amplified from pCMV-PE^{SpRY}, and NpuN, were then inserted downstream of GFP to obtain pAAV-EF1α-GFP-P2A-SpRY(H840A)$^{1\text{-}713}$-NpuN. NpuC and SpRY(H840A)$^{714\text{-}1368}$-M-MLV from pCMV-PE2 (SpRY) were subcloned to replace GFP to obtain pAAV-EF1α-NpuC-SpRY(H840A)$^{714\text{-}1368}$-M-MLV. All pegRNA and ngRNA constructs were generated by ligation of annealed oligos into pU6 expression plasmids and cloned into the modified pAAV-EF1α-GFP-P2A-SpRY(H840A)$^{1\text{-}713}$-NpuN with KpnI and NheI restriction sites for the insertions of U6-pegRNA and U6-ngRNA cassettes (see supplemental sequences and notes in Data S2).

Cell culture and transfection

Engineered mouse Neuro2a cell line carrying the *Pde6b*^{rd10} mutation (referred to as Neuro2a^{rd10}) was commercially established (InteRevo) and propagated in DMEM supplemented with 10% FBS (Gibco), 1% *L*-glutamine (Gibco), 100 mg/ml streptomycin, and 100 U/ml penicillin (Hyclone) at 37°C in a humidified condition with 5% CO_2. Cells were seeded on 24-well plates (Corning) for 18–24 h of growth at ∼60% confluency. The plasmids (1 μg/well) were transfected with Lipofectamine 3000 (Life Technologies) according to the manufacturer's protocol. Cells were cultured for 3 d, followed by harvesting for genomic DNA extraction.

Genomic DNA extraction

The genomic DNA from cells or retinas was extracted using the DNeasy Blood & Tissue kit (Qiagen) according to the manufacturer's protocol. All DNA samples were measured for concentration using Nanodrop (Thermo Fisher Scientific) and then subjected to PCR for restriction assays or targeted deep sequencing.

Off-target analysis

CIRCLE-seq was carried out to identify potential off-target sites experimentally. CIRCLE-seq library preparation was performed using genomic DNA extracted from untreated *Pde6b*^{rd10} mouse retina. In brief, genomic DNA was extracted using the TIANamp Genomic DNA Kit (TIANGEN) and fragmented to an average size of 300 bp using a Covaris E200 instrument. HTP Library Preparation Kit (KAPA Biosystems) was used for end repairs, A tailing, and stem-loop adaptor ligation. Adaptor-ligated DNA with a free 5′ phosphate was degraded away by treatment with Lambda Exonuclease and *Escherichia coli* Exonuclease (NEB). The genomic DNA was intramolecularly circularized using T4 DNA ligase (NEB), and any leftover linear double-stranded DNA was digested using Plasmid-Safe ATP-dependent DNase (Biosearch Technologies). Circularized DNA was subsequently treated with recombinant SpRY nuclease complexing with p5 and n3 gRNAs in a 50 μl volume for in vitro cleavage operations. After adapter ligation (NEB), the digested products were amplified by PCR using barcoded universal primers (NEBNext Multiplex Oligos for Illumina) and Kapa HiFi Polymerase (KAPA Biosystems). Libraries were quantified by quantitative PCR (Bio-Rad) and diluted to a final concentration of 15 pM for sequencing with 150-bp paired-end reads (Illumina). Data were processed using open-source CIRCLE-seq analysis pipeline (https://github.com/tsailabSJ/circleseq, version 1.1) with default parameters. The five top-ranking off-target loci discovered by CIRCLE-seq

analysis were selected for PCR amplification and high-throughput sequencing.

High-throughput targeted sequencing and data analysis

Genomic sites of interest were amplified from the extracted genomic DNA using the primers listed in Table S8. The amplicons were purified using QIAquick Gel Extraction Kit (Qiagen), and DNA concentration was measured using Nanodrop (Thermo Fisher Scientific). The pooled amplicons were sequenced with 150-bp paired-end reads on an Illumina Novaseq 6000 platform by Annoroad according to the manufacturer's protocols. Raw reads were filtered and analyzed using CRISPResso2 software package (Clement et al., 2019). To quantify the insertion–deletions frequencies of intentional and unpremeditated edits, paired-end sequencing files were aligned to a reference sequence using web-based tool Cas-analyzer (http://www.rgenome.net). Deep sequencing data are available from the NCBI Sequence Read Archive under accession number PRJNA784338.

AAV production

AAV vectors (InteRevo) were produced as previously described (Yao et al., 2018). Briefly, HEK293T cells (ATCC, authenticated by AAV production and tested for mycoplasma contamination by PCR) were cotransfected with plasmids for Rep/Cap (2/8) and genes of interest along with Helper plasmid. Cells were harvested 48 h after transfection and lysed with lysis buffer. After treatment with Benzonase (Sigma-Aldrich), the supernatants were ultracentrifuged in iodixanol gradient for purification. Purified AAVs were then concentrated with Amicon Ultra-15 Filter Units (Millipore) to a final titer of 4.0–6.0 × 10^{13} vg ml^{-1} (Table S7).

Subretinal injection

Mice were anesthetized and subjected to subretinal injections under a surgical microscope. An incision was made through the cornea at the nasal side using a sterile and beveled 30-gauge needle. Subretinal injection was carried out through a microsyringe equipped with a 32-gauge blunt-end needle (Hamilton), which was passed through the retina while avoiding the lens. Each eye received 0.7 µl of AAVs (approximately equal to 10^{13}–10^{14} vg kg^{-1} body weight) with Fastgreen (0.1%; Sigma-Aldrich) included in the suspension for visualization. Unless otherwise stated, the retinas of *Pde6b*^{rd10} mice treated with AAV vectors packaging split PE^{SpRY} and gScrambled/GFP were referred to as *Pde6b*^{rd10} control and those with packaging split PE^{SpRY} and g*Pde6b*/GFP were referred to as *Pde6b*$^{T\ to\ C}$ or *Pde6b*^{AGA}.

Retinal cell dissociation and FACS

Retinas were dissected out and incubated at 37°C for 20 min in the thermomixer with the activated Papain mix composed of 40 µl Papain (500 U/ml; Worthington), 40 µl Cysteine/EDTA mix (25 mM cysteine + 5 mM EDTA [pH 7.0]), and 320 µl HBSS/Hepes (normal HBSS + 10 mM Hepes). The cell pellet was collected and treated with benzonase at 37°C for 8 min. After the removal of supernatant, dissociated cells were resuspended in an appropriate volume of DPBS (Gibco). GFP$^+$ cells were sorted using a FACSAria cell sorter (BD Biosciences) and collected for genomic extraction.

H&E staining

Retinas were separated from the enucleated eyes and subjected to fixation in 4% paraformaldehyde for 30 min. After dehydration with a series of increasing ethanol concentrations (70, 95, and 100%) and incubation in xylene, retinas were embedded in paraffin and sectioned at 5 µm thickness with Leica microtome. Following the deparaffinization and rehydration, the slides with retinal sections were stained with H&E and mounted with Canada balsam (Sigma-Aldrich). Images were captured with an Olympus IX83 microscope.

Immunohistochemistry and imaging

Mice were anesthetized for perfusion with 4% paraformaldehyde, and eyes were enucleated. Retinas were then dissected carefully with forceps and postfixed in 4% paraformaldehyde for 30 min. After removal of the lens, the retinas were immersed in 30% sucrose and OCT (Leica). The embedded retinas were then cryo-sectioned at 20 µm thickness by Leica CM1950. Slides with retinal sections were washed with PBS and incubated with a blocking buffer containing 5% normal donkey serum (Jackson ImmunoResearch), 0.1% Triton X-100, and 0.1% NaN_3 in PBS for 1 h at room temperature. After overnight incubation with primary antibodies at 4°C, sections were washed PBS three times and then incubated with secondary antibodies in the humidified dark box for 2 h at room temperature. The nuclei were counterstained with DAPI (Sigma-Aldrich) and sections were mounted with Fluoromount G (SouthernBiotech). All antibodies used in this study are shown in Table S9.

Confocal images were acquired with Olympus FV3000 microscope. All images were taken under non-saturated conditions, and images to be compared were acquired with the same settings. The quantitative analysis of fluorescence intensity at each region of interest across the images was carried out by using ImageJ. The mean fluorescence intensities were calculated using the integrated "Analyze–Measure" tool of ImageJ, and statistical analysis was performed using Prism 8 (GraphPad).

Retinal flatmount

Retinal flatmounts were prepared as previously described (Yao et al., 2016). In brief, anesthetized mice were perfused with 4% paraformaldehyde, and eyes were enucleated. Retinas were then dissected carefully with forceps and postfixed in 4% paraformaldehyde for 30 min. After removal of the lens, the retinas were washed with PBS three times and flat-mounted in Fluoromount G (SouthernBiotech), with photoreceptor layers facing up or subjected to further immunostaining prior to mounting.

PDE activity assays

Retinas were isolated from the light-adapted mice and homogenized with ice-cold PDE Assay Buffer (BioVision) supplemented with Halt Protease Inhibitor Cocktail (Thermo Fisher Scientific). The PDE activity was measured with Total Phosphodiesterase Activity Assay Kit (BioVision) according to the manufacturer's

instructions. The fluorescence from the cleaved PDE substrates was recorded at Ex/Em 370/450 nm on a kinetic mode using SpectraMax iD5 (Molecular Devices), and the PDE activities were expressed as microunits per milligram retinal proteins.

Total cGMP assays

Retinas were isolated under infrared illumination or normal room light and homogenized in 100 µl lysis buffer (Cell Signaling Technology). Total cGMP amount was assayed in triplicate with cGMP XP Assay Kit (Cell Signaling Technology) according to the manufacturer's protocols. The absorbance at 450 nm was read using SpectraMax iD5 (Molecular Devices) and the cGMP levels were expressed as nmols cGMP per microgram total retinal proteins.

Western blotting

Cells or retinas were lysed and homogenized in radioimmunoprecipitation assay buffer (Yeasen) supplemented with Halt Protease Inhibitor Cocktail (Thermo Fisher Scientific). Samples were then centrifuged for 10 min at 4°C and the supernatants were collected and stored at −80°C for further assays. Protein concentrations were determined with BCA Protein Assay Kit (BioVision) using SpectraMax iD5 (Molecular Devices). Western blotting was performed essentially according to our previous report (Yao et al., 2014). In brief, samples were stacked and separated in 4 and 10% SDS gels, respectively, in running buffer (25 mM Tris base, 0.2 M glycine, 0.1% [wt/vol] SDS) with Mini-PROTEAN Tetra Cell system (Bio-Rad), followed by blotting on a PVDF membrane (Millipore). After blocking with 5% milk in TBST (200 mM Tris base, 1.36 M NaCl, pH 7.6, 0.1% [wt/vol] Tween 20) at room temperature for 1 h, the membrane was incubated with primary antibody at 4°C overnight. The membrane was then incubated with HRP-conjugated secondary antibody at room temperature for 1 h after washing, followed by immunodetection with SuperSignal West Femto (Thermo Fisher Scientific) on ChemiDoc Imaging System (Bio-Rad). All antibodies used in this study are shown in Table S9.

ERGs

Mice were anesthetized and pupils were dilated with 1% Tropicamide and 1% Atropine. ERGs (RetiMINER-C, IRC) were recorded from the corneal surface using a pair of platinum loop electrodes, along with a ground electrode placed in the tail and a reference electrode in the anterior scalp between the eyes. A drop of Genteal Gel (Alcon) was placed on the cornea to keep it moistened. For scotopic ERG, mice were dark-adapted overnight and stimulated with flashes of steadily increasing light intensity (−3.6, −2.6, −1.6, −0.6, 0.4, 1.4, and 2.15 log cds/m^2). For photopic ERG, mice were light-adapted for 10 min and stimulated with flashes (−0.6, 0, 0.6, 1, 1.4, and 2.15 log cds/m^2) while white background light (30 cds/m^2) was presented concomitantly. The band-pass filter was set between 0.3 and 300 Hz, and responses were averaged from 10 single flashes. All data were analyzed via RetiMINER4.0.

Light–dark transition test

The apparatus used for the light–dark transition test consisted of a box divided into a small (one-third) dark compartment and a large (two-thirds) illuminated compartment with varying luminance (300, 600, or 900 lux) connected by a small opening. Mice were initially released into the light compartment, facing away from the opening, and they moved freely between the two compartments for 5 min. The behavioral parameters including the time spent, distance traveled, rearing time, maximal or minimal visit time spent, total number of transitions, as well as mean velocity in light and dark compartments were automatically analyzed (SuperMaze, XINRUN) based on the behavior recorded by the camera of Light-Dark Box System XR-XB120 (XINRUN). After each trial, the compartments were cleaned with 70% ethanol and water to remove the olfactory cues.

Shuttle box learning test

Shuttle box test was carried out essentially as previously described (Masu et al., 1995). In brief, the apparatus consisted of a box divided into two equal compartments connected by a small opening. Each trial started with a light (20 cd/m^2) switched on selectively in the two compartments as a conditioned stimulus. The mouse could avoid foot shock (0.3 mA) applied continuously to the grid floor within 10 s after light exposure, which was regarded as active avoidance. If failed, the mouse could escape into the safe compartment once shocked, which was passive avoidance. The foot shock would last 3 s in the case of unsuccessful escape. Mice were subjected to daily training sessions of 100 trials for 5 d with the aim of avoidance learning acquisition, then followed by the tests at 1, 2, and 3 wk as well. The behavior of each mouse was recorded by the camera and automatically analyzed (SuperAPAS, XINRUN) with Shuttle Box System XR-XC404 (XINRUN) for a panel of parameters including the number and average response time of active or passive avoidance, the latency for the first active or passive avoidance, distance traveled, time spent, as well as shuttle times.

Optomotor response test

The optomotor reflex was assessed by an automated head-tracking system modified from a version previously published (Kretschmer et al., 2015). Mice were placed and freely moving on a central, elevated platform and presented with vertical sinusoidal grating stimuli rotating (12°/s) horizontally in either a clockwise or counterclockwise direction randomly generated by a virtual cylinder projected onto the four surrounding LCD monitors. The visual stimuli were presented either at maximum contrast (100%) with six different spatial frequencies (0.02, 0.1, 0.15, 0.2, 0.3, and 0.4 cycles/°) or at optimal spatial frequency (0.2 cycles/°) with six different contrasts (100, 50, 25, 12.5, 10, and 5%). Stimulus at each spatial frequency or contrast level lasted 50 s and presented in a randomized order and direction. Each mouse was tested for at least 12 trials and the performances were averaged for analysis.

The visual stimuli–elicited head movements were recorded by a camera placed above the animal and analyzed by an algorithm automatically tracking the position of the mouse head (OptoTrack XR-OT101 system, OptoTrack Version 4, XINRUN). The angles of the head in relation to the moving grating stimulus were therefore able to be automatically calculated for the measurements objectively obtained, which excluded

any subjective input from a human observer. The optomotor response was determined and quantified by calculating the ratio of the total amount of time (converted to the sum of frames in the algorithms) the animal head moved in the stimulus and in the opposite direction ($T_{correct}/T_{incorrect}$, thereafter named OMR) as conventionally used. In addition, based on the observation that in totally blind mice the differences between the head moving time in two directions were close or equal to 0, we, therefore, calculated $T_{correct} - T_{incorrect}$, referred to hereafter as ΔT, as a more intuitive way to measure the visual function.

Water-maze visual discrimination task

Visual function was assessed through a computer-based, two-alternative, forced-choice visual water-maze task as previously described (Prusky et al., 2000). The apparatus consisted of a trapezoidal-shaped pool with a release chute centered at the narrow end and a midline divider extending from the wide end into the pool. Positioned side by side at the wide end, two identical computer monitors faced into the pool and were calibrated for equal screen brightness. A vertical sinusoidal grating visual stimulus was presented on either monitor with the other displaying uniform gray. In terms of the test procedure, mice were shaped steadily through training under the optimal condition (100% contrast and 0.2 cycles/° spatial frequency) to swim from the release chute to the monitors and to associate the sinusoidal grating on the monitor with a submerged hidden platform that allowed them to escape from the water. Following a four-session daily training for four consecutive days (D1S1–D4S4), mice were afterward detected for visual function either at maximum contrast (100%) with a panel of spatial frequencies (0.05, 0.1, 0.2, 0.3, 0.4, and 0.5 cycles/°) or at optimal spatial frequency (0.2 cycles/°) with defined contrast levels (100, 50, 25, 10, 5, and 2%). Each visual test session consisted of 10 trials with the gratings presented in a pseudo-random pattern, LRLLRLRRLR (L or R, grafting displayed on left or right monitor), and a correct trial was scored when a mouse reached the platform without entry into the gray-displaying monitor side. The number of correct trials was expressed as percentage, and mice were considered to have learned the task when they achieved >70% correct choices. All trials were recorded by a camera and analyzed with Visu Water Task System (XR-OF801, XINRUN) for a panel of parameters including the latency time and distance traveled to find the platform.

Statistics

Statistical differences between different experimental groups were typically analyzed by a Student's *t* test, one-way ANOVA, or two-way ANOVA tests with Tukey's multiple comparisons. Data are presented as mean ± SEM and a value of $P < 0.05$ was considered significant. All experiments were independently performed at least three times to ensure repeatable results.

Online supplemental material

Fig. S1 shows diverse in vitro genome editing implemented by PE^{SpRY} system. Fig. S2 shows that PE^{SpRY} system elicits in vivo targeted genome editing at *Pde6b* locus. Fig. S3 shows immunohistochemistry in wild-type retinas and the preservative effects in the $Pde6b^{rd10}$ mice treated at P21 with PE^{SpRY} system and g*Pde6b*. Fig. S4 shows ERG responses in $Pde6b^{rd10}$ control mice at different ages, in $Pde6b^{AGA}$ mice, and in the $Pde6b^{rd10}$ mice treated at P21 with PE^{SpRY} system and g*Pde6b*. Fig. S5 shows the visual stimuli–driven optomotor responses in wild-type and $Pde6b^{rd10}$ control mice and mouse performance in water task. Table S1 shows sequences of p1–p14 gRNAs. Table S2 shows sequences of ngRNA n1–n7 and the distance from the target T•A base pair. Table S3 shows sequences of pegRNAs for optimization of RT templates and PBS lengths. Table S4 shows sequences of pegRNAs for diverse editings with optimized RT templates and PBS. Table S5 shows sequences of pegRNAs and ngRNAs for PE^{SpCas9} genome editing. Table S6 shows sequences of pegRNAs for in vivo genome editing in $Pde6b^{rd10}$ mice. Table S7 shows viral constructs, Rep/Cap, and virus titers. Table S8 shows primers used in the study. Table S9 shows antibodies used for immunohistochemistry and Western blotting. Data S1 show the sequences of indels for the pegRNA or ngRNA in the treated retinas. Data S2 show the sequences of constructs used in this study. Supplemental notes in Data S2 show the cloning protocol of the constructs.

Acknowledgments

We specifically acknowledge Prof. Haiwei Xu from Southwest Hospital at the Third Military Medical University for experimental help. We thank Prof. Ming-an Sun from the Institute of Comparative Medicine at Yangzhou University for advice with data analysis. We also thank members of Yao laboratory, including Caiyan Zheng, Yaqin Zhao, Lin Yan, Fang Xu, and Zihao Yang for their technical assistance.

This work was supported by the National Natural Science Foundation of China (no. 31970930, no. 32100936), the Hubei Natural Science Foundation (no. 2020CFA069, no. 2018CFB434), and the Neuroscience Team Development Project of Wuhan University of Science and Technology (no. 1180002).

Author contributions: H. Qin and W. Zhang performed experiments and analyzed data. S. Zhang and J. Zhang performed ERG, light–dark transition test, and shuttle box learning test. Y. Feng and X. Fu performed deep sequencing and analyzed data. W. Xu, S. Liu, and Z. Xu performed optomotor response test and water-maze visual discrimination task. J. Qi and Y. Lei performed cell experiments and image acquisition via confocal microscope. Q. Zhang and J. Wang performed PDE and cGMP assays, Western blotting, and subretinal injection. C. Xu and S. Feng performed perfusion, retinal cryo-section, retinal flatmount preparation, and immunohistochemistry. W. Liu and P. Li performed cell experiments and made figures. H. Qin, W. Zhang, and K. Yao conceived the project. K. Yao supervised the research and wrote the manuscript. All authors discussed the experiments and made comments on the manuscript.

Disclosures: The authors declare no competing interests exist.

Submitted: 4 May 2022
Revised: 23 December 2022
Accepted: 8 February 2023

References

Anzalone, A.V., X.D. Gao, C.J. Podracky, A.T. Nelson, L.W. Koblan, A. Raguram, J.M. Levy, J.A.M. Mercer, and D.R. Liu. 2022. Programmable deletion, replacement, integration and inversion of large DNA sequences with twin prime editing. *Nat. Biotechnol.* 40:731–740. https://doi.org/10.1038/s41587-021-01133-w

Anzalone, A.V., L.W. Koblan, and D.R. Liu. 2020. Genome editing with CRISPR-Cas nucleases, base editors, transposases and prime editors. *Nat. Biotechnol.* 38:824–844. https://doi.org/10.1038/s41587-020-0561-9

Anzalone, A.V., P.B. Randolph, J.R. Davis, A.A. Sousa, L.W. Koblan, J.M. Levy, P.J. Chen, C. Wilson, G.A. Newby, A. Raguram, and D.R. Liu. 2019. Search-and-replace genome editing without double-strand breaks or donor DNA. *Nature.* 576:149–157. https://doi.org/10.1038/s41586-019-1711-4

Banskota, S., A. Raguram, S. Suh, S.W. Du, J.R. Davis, E.H. Choi, X. Wang, S.C. Nielsen, G.A. Newby, P.B. Randolph, et al. 2022. Engineered virus-like particles for efficient in vivo delivery of therapeutic proteins. *Cell.* 185: 250–265.e16. https://doi.org/10.1016/j.cell.2021.12.021

Cebrian-Serrano, A., and B. Davies. 2017. CRISPR-cas orthologues and variants: Optimizing the repertoire, specificity and delivery of genome engineering tools. *Mamm. Genome.* 28:247–261. https://doi.org/10.1007/s00335-017-9697-4

Chang, B., N.L. Hawes, M.T. Pardue, A.M. German, R.E. Hurd, M.T. Davisson, S. Nusinowitz, K. Rengarajan, A.P. Boyd, S.S. Sidney, et al. 2007. Two mouse retinal degenerations caused by missense mutations in the beta-subunit of rod cGMP phosphodiesterase gene. *Vis. Res.* 47:624–633. https://doi.org/10.1016/j.visres.2006.11.020

Chatterjee, P., N. Jakimo, J. Lee, N. Amrani, T. Rodríguez, S.R.T. Koseki, E. Tysinger, R. Qing, S. Hao, E.J. Sontheimer, and J. Jacobson. 2020a. An engineered ScCas9 with broad PAM range and high specificity and activity. *Nat. Biotechnol.* 38:1154–1158. https://doi.org/10.1038/s41587-020-0517-0

Chatterjee, P., J. Lee, L. Nip, S.R.T. Koseki, E. Tysinger, E.J. Sontheimer, J.M. Jacobson, and N. Jakimo. 2020b. A Cas9 with PAM recognition for adenine dinucleotides. *Nat. Commun.* 11:2474. https://doi.org/10.1038/s41467-020-16117-8

Chen, Y., S. Zhi, W. Liu, J. Wen, S. Hu, T. Cao, H. Sun, Y. Li, L. Huang, Y. Liu, et al. 2020. Development of highly efficient dual-AAV split adenosine base editor for in vivo gene therapy. *Small Methods.* 4:2000309. https://doi.org/10.1002/smtd.202000309

Chew, W.L., M. Tabebordbar, J.K. Cheng, P. Mali, E.Y. Wu, A.H. Ng, K. Zhu, A.J. Wagers, and G.M. Church. 2016. A multifunctional AAV-CRISPR-Cas9 and its host response. *Nat. Methods.* 13:868–874. https://doi.org/10.1038/nmeth.3993

Choi, E.H., S. Suh, A.T. Foik, H. Leinonen, G.A. Newby, X.D. Gao, S. Banskota, T. Hoang, S.W. Du, Z. Dong, et al. 2022. In vivo base editing rescues cone photoreceptors in a mouse model of early-onset inherited retinal degeneration. *Nat. Commun.* 13:1830. https://doi.org/10.1038/s41467-022-29490-3

Clement, K., H. Rees, M.C. Canver, J.M. Gehrke, R. Farouni, J.Y. Hsu, M.A. Cole, D.R. Liu, J.K. Joung, D.E. Bauer, and L. Pinello. 2019. CRISPResso2 provides accurate and rapid genome editing sequence analysis. *Nat. Biotechnol.* 37:224–226. https://doi.org/10.1038/s41587-019-0032-3

Daiger, S.P., L.S. Sullivan, and S.J. Bowne. 2013. Genes and mutations causing retinitis pigmentosa. *Clin. Genet.* 84:132–141. https://doi.org/10.1111/cge.12203

Davis, J.R., X. Wang, I.P. Witte, T.P. Huang, J.M. Levy, A. Raguram, S. Banskota, N.G. Seidah, K. Musunuru, and D.R. Liu. 2022. Efficient in vivo base editing via single adeno-associated viruses with size-optimized genomes encoding compact adenine base editors. *Nat. Biomed. Eng.* 6: 1272–1283. https://doi.org/10.1038/s41551-022-00911-4

Gagliardi, G., K. Ben M'Barek, and O. Goureau. 2019. Photoreceptor cell replacement in macular degeneration and retinitis pigmentosa: A pluripotent stem cell-based approach. *Prog. Retin. Eye Res.* 71:1–25. https://doi.org/10.1016/j.preteyeres.2019.03.001

Gao, L., D.B.T. Cox, W.X. Yan, J.C. Manteiga, M.W. Schneider, T. Yamano, H. Nishimasu, O. Nureki, N. Crosetto, and F. Zhang. 2017. Engineered Cpf1 variants with altered PAM specificities. *Nat. Biotechnol.* 35:789–792. https://doi.org/10.1038/nbt.3900

Gaudelli, N.M., A.C. Komor, H.A. Rees, M.S. Packer, A.H. Badran, D.I. Bryson, and D.R. Liu. 2017. Programmable base editing of A•T to G•C in genomic DNA without DNA cleavage. *Nature.* 551:464–471. https://doi.org/10.1038/nature24644

Hartong, D.T., E.L. Berson, and T.P. Dryja. 2006. Retinitis pigmentosa. *Lancet.* 368:1795–1809. https://doi.org/10.1016/S0140-6736(06)69740-7

Hille, F., H. Richter, S.P. Wong, M. Bratovič, S. Ressel, and E. Charpentier. 2018. The biology of CRISPR-Cas: Backward and forward. *Cell.* 172: 1239–1259. https://doi.org/10.1016/j.cell.2017.11.032

Hirano, S., H. Nishimasu, R. Ishitani, and O. Nureki. 2016. Structural basis for the altered PAM specificities of engineered CRISPR-Cas9. *Mol. Cell.* 61: 886–894. https://doi.org/10.1016/j.molcel.2016.02.018

Hu, J.H., S.M. Miller, M.H. Geurts, W. Tang, L. Chen, N. Sun, C.M. Zeina, X. Gao, H.A. Rees, Z. Lin, and D.R. Liu. 2018. Evolved Cas9 variants with broad PAM compatibility and high DNA specificity. *Nature.* 556:57–63. https://doi.org/10.1038/nature26155

Jacobson, S.G., A.V. Cideciyan, A.J. Roman, A. Sumaroka, S.B. Schwartz, E. Heon, and W.W. Hauswirth. 2015. Improvement and decline in vision with gene therapy in childhood blindness. *N. Engl. J. Med.* 372: 1920–1926. https://doi.org/10.1056/NEJMoa1412965

Jang, H., D.H. Jo, C.S. Cho, J.H. Shin, J.H. Seo, G. Yu, R. Gopalappa, D. Kim, S.R. Cho, J.H. Kim, and H.H. Kim. 2021. Application of prime editing to the correction of mutations and phenotypes in adult mice with liver and eye diseases. *Nat. Biomed. Eng.* 6:181–194. https://doi.org/10.1038/s41551-021-00788-9

Jo, D.H., D.W. Song, C.S. Cho, U.G. Kim, K.J. Lee, K. Lee, S.W. Park, D. Kim, J.H. Kim, J.S. Kim, et al. 2019. CRISPR-Cas9-mediated therapeutic editing of Rpe65 ameliorates the disease phenotypes in a mouse model of Leber congenital amaurosis. *Sci. Adv.* 5:eaax1210. https://doi.org/10.1126/sciadv.aax1210

Kim, H.K., S. Lee, Y. Kim, J. Park, S. Min, J.W. Choi, T.P. Huang, S. Yoon, D.R. Liu, and H.H. Kim. 2020. High-throughput analysis of the activities of xCas9, SpCas9-NG and SpCas9 at matched and mismatched target sequences in human cells. *Nat. Biomed. Eng.* 4:111–124. https://doi.org/10.1038/s41551-019-0505-1

Kleinstiver, B.P., V. Pattanayak, M.S. Prew, S.Q. Tsai, N.T. Nguyen, Z. Zheng, and J.K. Joung. 2016. High-fidelity CRISPR-Cas9 nucleases with no detectable genome-wide off-target effects. *Nature.* 529:490–495. https://doi.org/10.1038/nature16526

Kleinstiver, B.P., M.S. Prew, S.Q. Tsai, V.V. Topkar, N.T. Nguyen, Z. Zheng, A.P.W. Gonzales, Z. Li, R.T. Peterson, J.R.J. Yeh, et al. 2015. Engineered CRISPR-Cas9 nucleases with altered PAM specificities. *Nature.* 523: 481–485. https://doi.org/10.1038/nature14592

Kleinstiver, B.P., A.A. Sousa, R.T. Walton, Y.E. Tak, J.Y. Hsu, K. Clement, M.M. Welch, J.E. Horng, J. Malagon-Lopez, I. Scarfò, et al. 2019. Engineered CRISPR-Cas12a variants with increased activities and improved targeting ranges for gene, epigenetic and base editing. *Nat. Biotechnol.* 37:276–282. https://doi.org/10.1038/s41587-018-0011-0

Koblan, L.W., M. Arbab, M.W. Shen, J.A. Hussmann, A.V. Anzalone, J.L. Doman, G.A. Newby, D. Yang, B. Mok, J.M. Replogle, et al. 2021. Efficient C•G-to-G•C base editors developed using CRISPRi screens, target-library analysis, and machine learning. *Nat. Biotechnol.* 39: 1414–1425. https://doi.org/10.1038/s41587-021-00938-z

Komor, A.C., Y.B. Kim, M.S. Packer, J.A. Zuris, and D.R. Liu. 2016. Programmable editing of a target base in genomic DNA without double-stranded DNA cleavage. *Nature.* 533:420–424. https://doi.org/10.1038/nature17946

Kretschmer, F., S. Sajgo, V. Kretschmer, and T.C. Badea. 2015. A system to measure the Optokinetic and Optomotor response in mice. *J. Neurosci. Methods.* 256:91–105. https://doi.org/10.1016/j.jneumeth.2015.08.007

Levy, J.M., W.H. Yeh, N. Pendse, J.R. Davis, E. Hennessey, R. Butcher, L.W. Koblan, J. Comander, Q. Liu, and D.R. Liu. 2020. Cytosine and adenine base editing of the brain, liver, retina, heart and skeletal muscle of mice via adeno-associated viruses. *Nat. Biomed. Eng.* 4:97–110. https://doi.org/10.1038/s41551-019-0501-5

Maeder, M.L., M. Stefanidakis, C.J. Wilson, R. Baral, L.A. Barrera, G.S. Bounoutas, D. Bumcrot, H. Chao, D.M. Ciulla, J.A. DaSilva, et al. 2019. Development of a gene-editing approach to restore vision loss in Leber congenital amaurosis type 10. *Nat. Med.* 25:229–233. https://doi.org/10.1038/s41591-018-0327-9

Masu, M., H. Iwakabe, Y. Tagawa, T. Miyoshi, M. Yamashita, Y. Fukuda, H. Sasaki, K. Hiroi, Y. Nakamura, R. Shigemoto, et al. 1995. Specific deficit of the ON response in visual transmission by targeted disruption of the mGluR6 gene. *Cell.* 80:757–765. https://doi.org/10.1016/0092-8674(95)90354-2

Miller, S.M., T. Wang, P.B. Randolph, M. Arbab, M.W. Shen, T.P. Huang, Z. Matuszek, G.A. Newby, H.A. Rees, and D.R. Liu. 2020. Continuous evolution of SpCas9 variants compatible with non-G PAMs. *Nat. Biotechnol.* 38:471–481. https://doi.org/10.1038/s41587-020-0412-8

Neugebauer, M.E., A. Hsu, M. Arbab, N.A. Krasnow, A.N. McElroy, S. Pandey, J.L. Doman, T.P. Huang, A. Raguram, S. Banskota, et al. 2022. Evolution of an adenine base editor into a small, efficient cytosine base editor with low off-target activity. *Nat. Biotechnol.* https://doi.org/10.1038/s41587-022-01533-6

Nishimasu, H., X. Shi, S. Ishiguro, L. Gao, S. Hirano, S. Okazaki, T. Noda, O.O. Abudayyeh, J.S. Gootenberg, H. Mori, et al. 2018. Engineered CRISPR-Cas9 nuclease with expanded targeting space. *Science*. 361:1259–1262. https://doi.org/10.1126/science.aas9129

Prusky, G.T., P.W. West, and R.M. Douglas. 2000. Behavioral assessment of visual acuity in mice and rats. *Vis. Res.* 40:2201–2209. https://doi.org/10.1016/S0042-6989(00)00081-X

Raguram, A., S. Banskota, and D.R. Liu. 2022. Therapeutic in vivo delivery of gene editing agents. *Cell*. 185:2806–2827. https://doi.org/10.1016/j.cell.2022.03.045

Redmond, T.M., S. Yu, E. Lee, D. Bok, D. Hamasaki, N. Chen, P. Goletz, J.X. Ma, R.K. Crouch, and K. Pfeifer. 1998. Rpe65 is necessary for production of 11-cis-vitamin A in the retinal visual cycle. *Nat. Genet.* 20:344–351. https://doi.org/10.1038/3813

Russell, S., J. Bennett, J.A. Wellman, D.C. Chung, Z.F. Yu, A. Tillman, J. Wittes, J. Pappas, O. Elci, S. McCague, et al. 2017. Efficacy and safety of voretigene neparvovec (AAV2-hRPE65v2) in patients with RPE65-mediated inherited retinal dystrophy: A randomised, controlled, open-label, phase 3 trial. *Lancet*. 390:849–860. https://doi.org/10.1016/S0140-6736(17)31868-8

Song, M., H.K. Kim, S. Lee, Y. Kim, S.Y. Seo, J. Park, J.W. Choi, H. Jang, J.H. Shin, S. Min, et al. 2020. Sequence-specific prediction of the efficiencies of adenine and cytosine base editors. *Nat. Biotechnol.* 38:1037–1043. https://doi.org/10.1038/s41587-020-0573-5

Suh, S., E.H. Choi, H. Leinonen, A.T. Foik, G.A. Newby, W.H. Yeh, Z. Dong, P.D. Kiser, D.C. Lyon, D.R. Liu, and K. Palczewski. 2021. Restoration of visual function in adult mice with an inherited retinal disease via adenine base editing. *Nat. Biomed. Eng.* 5:169–178. https://doi.org/10.1038/s41551-020-00632-6

Trapani, I., A. Puppo, and A. Auricchio. 2014. Vector platforms for gene therapy of inherited retinopathies. *Prog. Retin. Eye Res.* 43:108–128. https://doi.org/10.1016/j.preteyeres.2014.08.001

Verbakel, S.K., R.A.C. van Huet, C.J.F. Boon, A.I. den Hollander, R.W.J. Collin, C.C.W. Klaver, C.B. Hoyng, R. Roepman, and B.J. Klevering. 2018. Non-syndromic retinitis pigmentosa. *Prog. Retin. Eye Res.* 66:157–186. https://doi.org/10.1016/j.preteyeres.2018.03.005

Walton, R.T., K.A. Christie, M.N. Whittaker, and B.P. Kleinstiver. 2020. Unconstrained genome targeting with near-PAMless engineered CRISPR-Cas9 variants. *Science*. 368:290–296. https://doi.org/10.1126/science.aba8853

Yao, K., S.W. Lau, and W. Ge. 2014. Differential regulation of Kit ligand A expression in the ovary by IGF-I via different pathways. *Mol. Endocrinol.* 28:138–150. https://doi.org/10.1210/me.2013-1186

Yao, K., S. Qiu, L. Tian, W.D. Snider, J.G. Flannery, D.V. Schaffer, and B. Chen. 2016. Wnt regulates proliferation and neurogenic potential of Müller Glial cells via a Lin28/let-7 miRNA-dependent pathway in adult mammalian retinas. *Cell Rep.* 17:165–178. https://doi.org/10.1016/j.celrep.2016.08.078

Yao, K., S. Qiu, Y.V. Wang, S.J.H. Park, E.J. Mohns, B. Mehta, X. Liu, B. Chang, D. Zenisek, M.C. Crair, et al. 2018. Restoration of vision after de novo genesis of rod photoreceptors in mammalian retinas. *Nature*. 560:484–488. https://doi.org/10.1038/s41586-018-0425-3

Yu, W., S. Mookherjee, V. Chaitankar, S. Hiriyanna, J.W. Kim, M. Brooks, Y. Ataeijannati, X. Sun, L. Dong, T. Li, et al. 2017. Nrl knockdown by AAV-delivered CRISPR/Cas9 prevents retinal degeneration in mice. *Nat. Commun.* 8:14716. https://doi.org/10.1038/ncomms14716

Zhi, S., Y. Chen, G. Wu, J. Wen, J. Wu, Q. Liu, Y. Li, R. Kang, S. Hu, J. Wang, et al. 2022. Dual-AAV delivering split prime editor system for in vivo genome editing. *Mol. Ther.* 30:283–294. https://doi.org/10.1016/j.ymthe.2021.07.011

JEM

Supplemental material

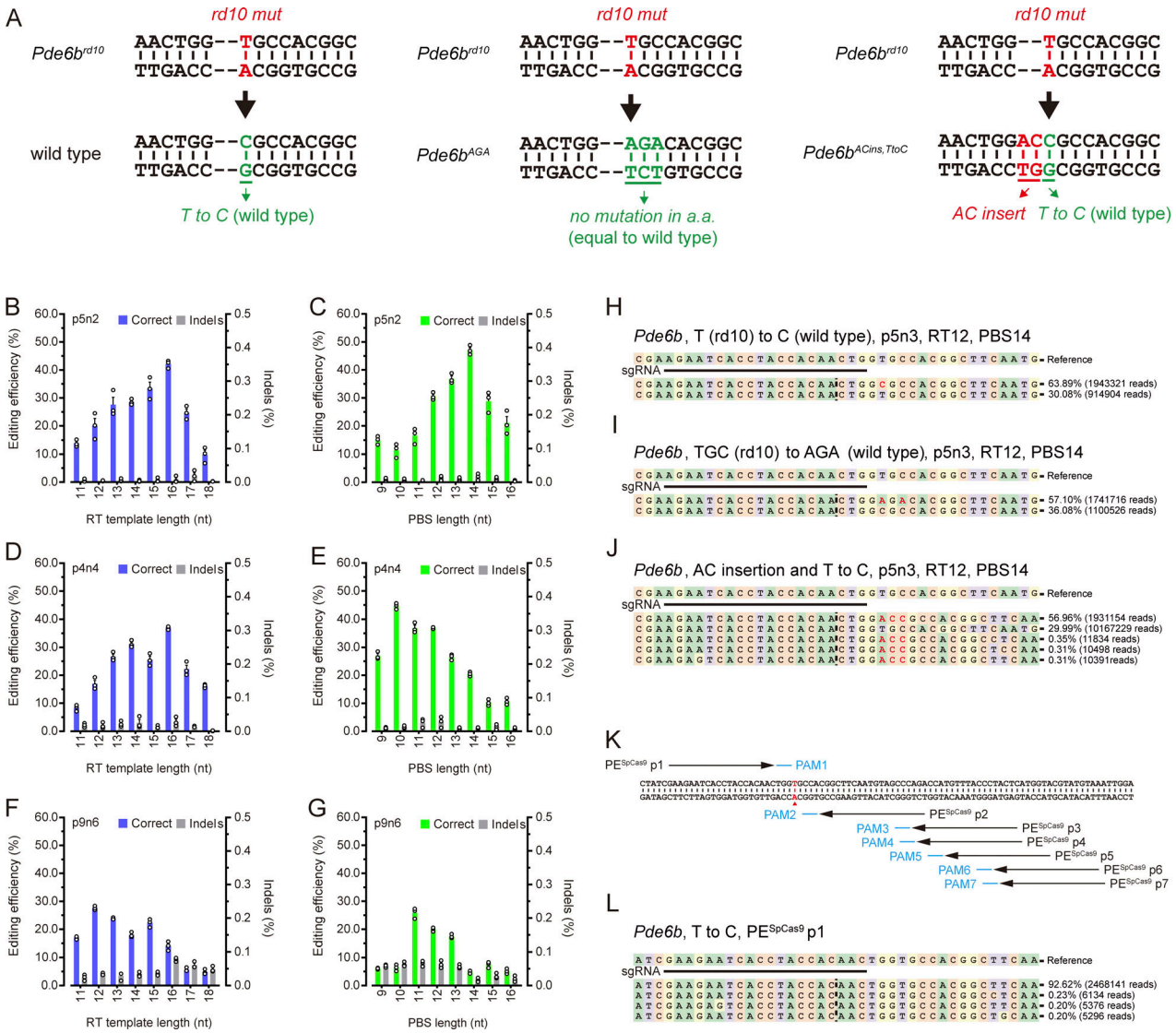

Figure S1. **Diverse in vitro genome editing implemented by PE^{SpRY} system. (A)** Three representative genome-editing types, referred to as *Pde6b*$^{T\ to\ C}$, *Pde6b*^{AGA}, and *Pde6b*$^{ACins,\ TtoC}$, respectively. **(B–G)** Editing efficiency of correct edits and indels for p5n2, p4n4, and p9n6 combination with varying RT template (B, D, and F) or PBS (C, E, and G) lengths. Data in B–G are presented as mean ± SEM; *n* = 3 independent biological replicates. All experiments were independently performed at least three times to ensure repeatable results. **(H–J)** PE^{SpRY} system–mediated on-target genome editing at *Pde6b* locus, validated by high-throughput sequencing. Alleles from genomic DNA isolated from Neuro2a^{rd10} cells after PE^{SpRY} system–mediated *Pde6b*$^{T\ to\ C}$ (H), *Pde6b*^{AGA} (I), *Pde6b*$^{ACins,\ TtoC}$ (J) editing with the p5n3 combination and with the optimized PBS and RT template lengths. Alleles were sequenced on an Illumina Novaseq 6000 platform and analyzed using CRISPResso2. The reference sequence from the amplified region and the gRNA sequence are at the top. Representative allele frequencies and corresponding sequencing reads are indicated for each allele. The alleles with a frequency ≥0.20% are shown. The nicking sites are indicated with a dashed line, and the intended editing is indicated in red. All experiments were independently performed at least three times to ensure repeatable results. **(K and L)** No targeted editing is elicited by PE^{SpCas9} at *Pde6b* locus. **(K)** Seven pegRNAs (PE^{SpCas9} p1–p7) neighboring the target T•A base pair are selected for PE^{SpCas9} system–mediated genome editing. The target T•A base pair is highlighted in red. PAMs are indicated in blue. **(L)** Alleles from genomic DNA isolated from engineered Neuro2a cells (Neuro2a^{rd10}) treated with PE^{SpCas9} and PE^{SpCas9} p1 gRNA (see Table S5). Alleles were sequenced on an Illumina Novaseq 6000 platform and analyzed using CRISPResso2. The reference sequence from the amplified region and the gRNA sequence is at the top. Representative allele frequencies and corresponding sequencing reads are indicated. The alleles with a frequency ≥0.20% are shown and the nicking sites are indicated with a dashed line. All experiments were independently performed at least three times to ensure repeatable results.

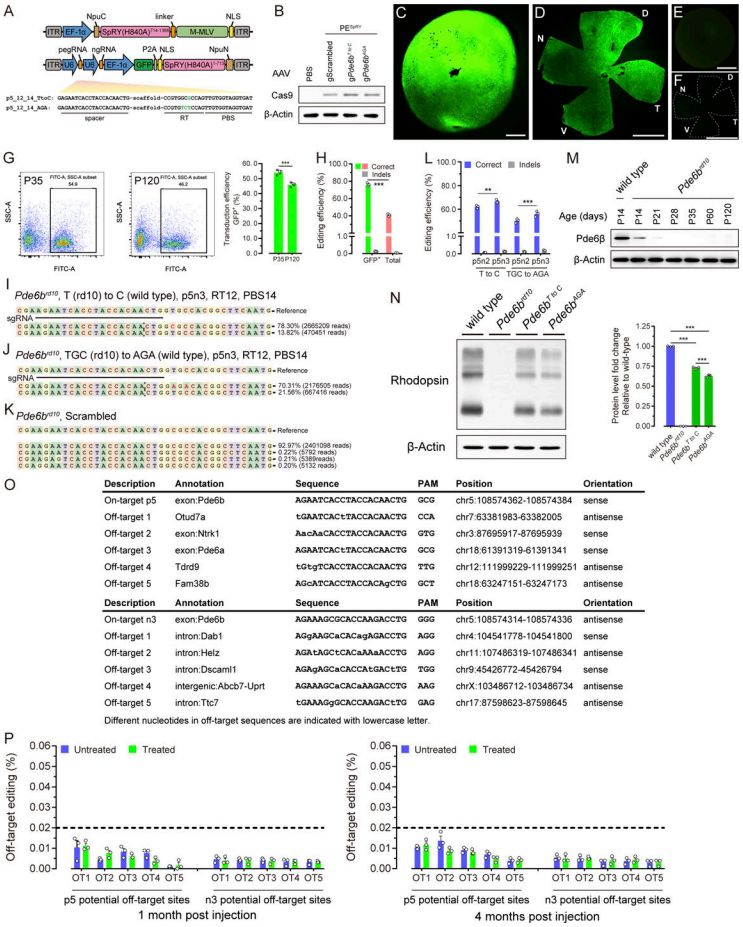

Figure S2. **PE^{SpRY} system elicits in vivo targeted genome editing at *Pde6b* locus. (A)** Schematic representations of the split Npu intein–based dual AAV system for the delivery of PE^{SpRY}, gRNAs (prime editing and ngRNAs) as well as GFP, and the pegRNA sequences used in in vivo study. The base pairs corresponding to the installed edits are indicated in green. **(B)** Detection of proteins expressed in the retinas by the transgene from AAV vectors. *Pde6b^{rd10}* mice were subretinally injected at P14 with PBS, or AAV vectors packaging split PE^{SpRY} and gScrambled, split PE^{SpRY} and *gPde6b$^{T\ to\ C}$*, or split PE^{SpRY} and *gPde6b^{AGA}*. Retinas were harvested at P35 and examined for immunoblotting assay by SpCas9 and β-Actin antibodies. **(C–F)** Retinas are transduced efficiently with a dual AAV system. Representative images of retinas transduced (C and D) or untransduced (E and F) were shown. GFP signals were examined right after the eyes were dissected (C and E) or in a flatmount preparation (D and F). D, dorsal; V, ventral; N, nasal; and T, temporal. Dashed lines in F indicate the profile of untransduced retina with fairly low fluorescence signal. Scale bars, 500 µm (C), 300 µm (D), 1,000 µm (E), 600 µm (F). **(G)** Quantification of GFP$^+$ cells by flow cytometry. Retinas transduced with vectors installing the edit of *Pde6b$^{T\ to\ C}$* were harvested at P35 and P120. Representative flow cytometry images are shown and the data are presented as mean ± SEM; *n* = 4 independent biological replicates, Student's two-tailed paired *t* test. ***, P < 0.001. **(H)** A comparison of editing efficiencies in sorted GFP$^+$ and total retinal cells. Retinas of *Pde6b$^{T\ to\ C}$* editing were harvested at P120. Representative data are presented as mean ± SEM; *n* = 3 independent biological replicates. Two-way ANOVA tests with Tukey's multiple comparisons. ***, P < 0.001. **(I–K)** Alleles from genomic DNA isolated from sorted GFP$^+$ retinal cells subjected to PE^{SpRY} system–mediated *Pde6b$^{T\ to\ C}$* (I) and *Pde6b^{AGA}* (J) editing with the p5n3 combination and the optimized PBS and RT template, and from sorted GFP$^+$ retinal cells of control retinas (K). Representative next-generation sequencing (NGS) results were shown. Alleles were sequenced on an Illumina Novaseq 6000 platform and analyzed using CRISPResso2. The reference sequence from the amplified region and the gRNA sequence is at the top. Representative allele frequencies and corresponding sequencing reads are indicated. The alleles with a frequency ≥0.20% are shown. The nicking sites are indicated with dashed line and the intended editing is indicated in red. **(L)** Frequencies of correct edits and indels in the total sequencing reads for *Pde6b$^{T\ to\ C}$* and *Pde6b^{AGA}* editing with p5n3 or p5n2 combinations and with the optimized PBS and RT template lengths in sorted GFP$^+$ retinal cells. Retinas were harvested at P35. Representative data are presented as mean ± SEM; *n* = 3 independent biological replicates. Two-way ANOVA tests with Tukey's multiple comparisons. **, P < 0.01; ***, P < 0.001. **(M)** Pde6β protein levels in *Pde6b^{rd10}* control retinas at different ages. Pde6β proteins were examined for retinal extracts from wild-type at P14 and *Pde6b^{rd10}* control retinas at P14, P21, P28, P35, P60, and P120. Representative immunoblotting images for Pde6β and β-Actin are shown in M, and the relative Pde6β protein levels of wild-type and *Pde6b^{rd10}* retinas at different ages were quantified in Fig. 2 D. **(N)** Rhodopsin protein levels in wild-type, *Pde6b^{rd10}*, *Pde6b$^{T\ to\ C}$*, and *Pde6b^{AGA}* retinas at P120. Rhodopsin proteins were examined for retinal extracts from wild-type, *Pde6b^{rd10}*, *Pde6b$^{T\ to\ C}$*, and *Pde6b^{AGA}* at P120. Representative immunoblotting images for Rhodopsin and β-Actin are shown in N, and the relative Rhodopsin protein levels of wild-type, *Pde6b^{rd10}*, *Pde6b$^{T\ to\ C}$*, and *Pde6b^{AGA}* retinas were quantified. Representative data are presented as mean ± SEM; *n* = 3 independent biological replicates. One-way ANOVA tests with Tukey's multiple comparisons. ***, P < 0.001. All of *Pde6b^{rd10}* control retinas were treated with PE^{SpRY} and gScrambled. **(O and P)** Off-target editing by PE^{SpRY} system in the treated retinas. **(O)** Potential off-target sites experimentally captured by CIRCLE-seq. Top five potential off-target sites for p5 pegRNA and n3 ngRNA were demonstrated. **(P)** Off-target editing frequencies of the treated retinas with the edit of *Pde6b$^{T\ to\ C}$*. Retinas were harvested at 1 or 4 mo after injection for off-target assays. The untreated retinas were from the age-matched *Pde6b^{rd10}* mice. The potential off-target sites for both of p5 pegRNA and n3 ngRNA were assayed using high-throughput targeted sequencing. Representative data are presented as mean ± SEM; *n* = 3 independent biological replicates. All experiments were independently performed at least three times to ensure repeatable results. Source data are available for this figure: SourceData FS2.

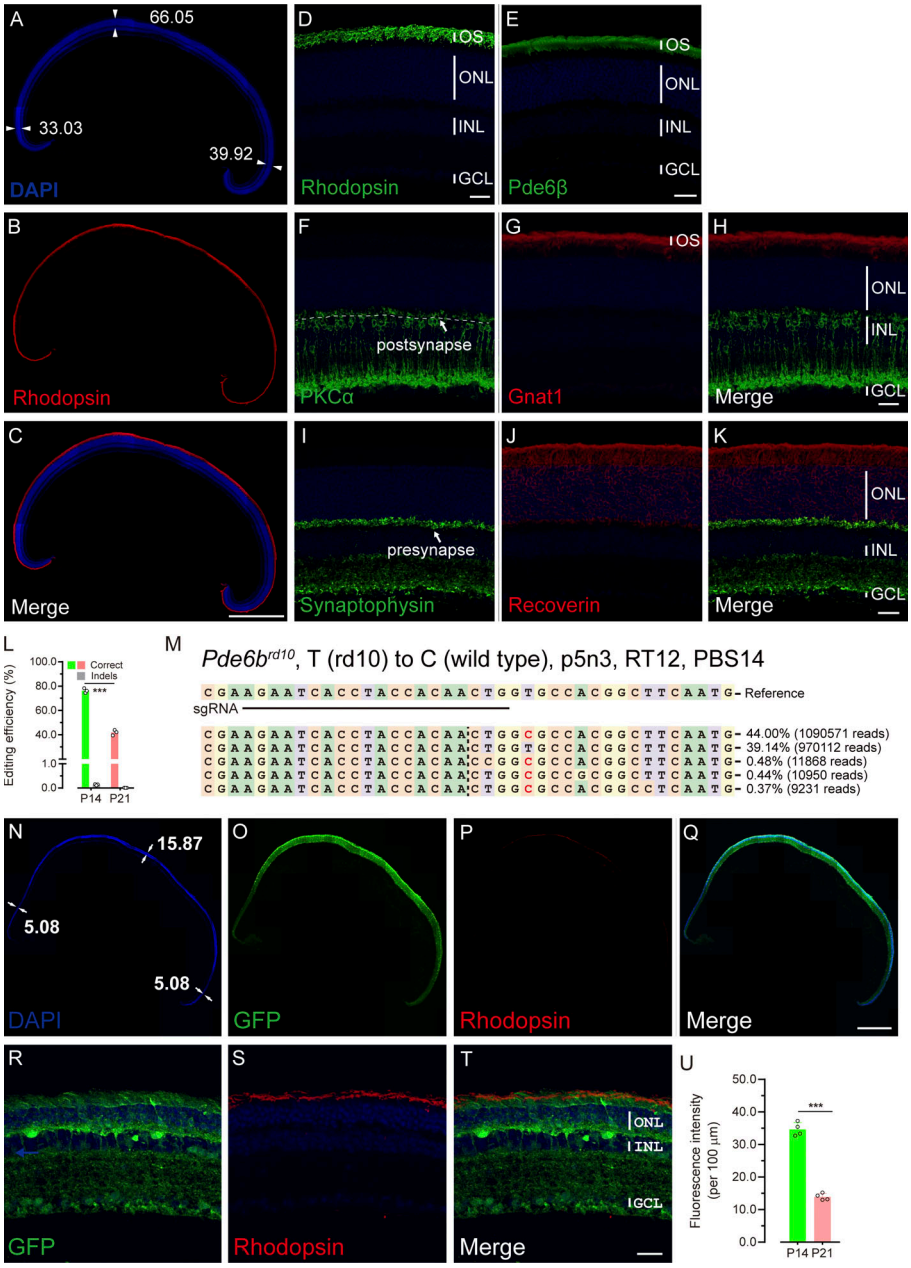

Figure S3. **Immunohistochemistry in wild-type retinas and the preservative effects in the *Pde6b*^{rd10} mice treated at P21 with PE^{SpRY} system and g*Pde6b*. (A–K)** Wild-type retinal sections were examined with antibodies for Rhodopsin (A–D), Pde6β (E), PKCα (F and H), Gnat1 (G and H), Synaptophysin (I and K), and Recoverin (J and K). Representative images were shown, and the fluorescence intensities for B, D–G, I, and J were quantified in Fig. 2, F and O; and Fig. 3, E, J, and M. Numbers in A present the thickness of the regions indicated with arrows. INL, inner nuclear layer; GCL, ganglion cell layer; OS, outer segment. Scale bars, 500 μm (A–C) or 20 μm (D–K). **(L–U)** The preservative effects in the *Pde6b*^{rd10} mice treated at P21 with PE^{SpRY} system and g*Pde6b*. **(L)** A comparison of editing efficiencies between treatment at P14 and P21. Representative editing frequencies of correct edits and indels for *Pde6b*$^{T\ to\ C}$ editing in the *Pde6b*^{rd10} mouse retinas treated with p5n3 combinations and with the optimized PBS and RT template lengths in sorted GFP$^+$ retinal cells were demonstrated. Data are presented as mean ± SEM; *n* = 3 independent biological replicates. Two-way ANOVA tests with Tukey's multiple comparisons. **(M)** Alleles from genomic DNA isolated from sorted GFP$^+$ retinal cells subjected to PE^{SpRY} system–mediated *Pde6b*$^{T\ to\ C}$ editing with the p5n3 combination and the optimized PBS and RT template. Representative NGS results were shown. Alleles were sequenced on an Illumina Novaseq 6000 platform and analyzed using CRISPResso2. The reference sequence from the amplified region and the gRNA sequence are at the top. Representative allele frequencies and corresponding sequencing reads are indicated. The alleles with a frequency ≥0.35% are shown. The nicking sites are indicated with dash line, and the intended editing is indicated in red. **(N–Q)** Rod photoreceptor preservation in the *Pde6b*$^{T\ to\ C}$ mice treated at P21. The retinas from *Pde6b*$^{T\ to\ C}$ mice were sectioned and raised for Rhodopsin antibody. Representative images were shown. Blue, DAPI; green, GFP; red, Rhodopsin. Numbers in N present the thickness of the regions indicated with arrows. Scale bars, 300 μm. **(R–T)** Examination of Rhodopsin immunohistochemistry with higher magnification for *Pde6b*$^{T\ to\ C}$ retinal sections. Representative images were shown. INL, inner nuclear layer; GCL, ganglion cell layer. Scale bars, 20 μm. **(U)** Fluorescence intensities of Rhodopsin immunohistochemistry of retinal sections from *Pde6b*$^{T\ to\ C}$ mice treated at P21 were quantified, in comparison with those from *Pde6b*$^{T\ to\ C}$ mice treated at P14. All of samples were harvested at P120. Representative data are presented as mean ± SEM; *n* = 4 independent biological replicates, Student's two-tailed paired *t* test. ***, P < 0.001. All experiments were independently performed at least three times to ensure repeatable results.

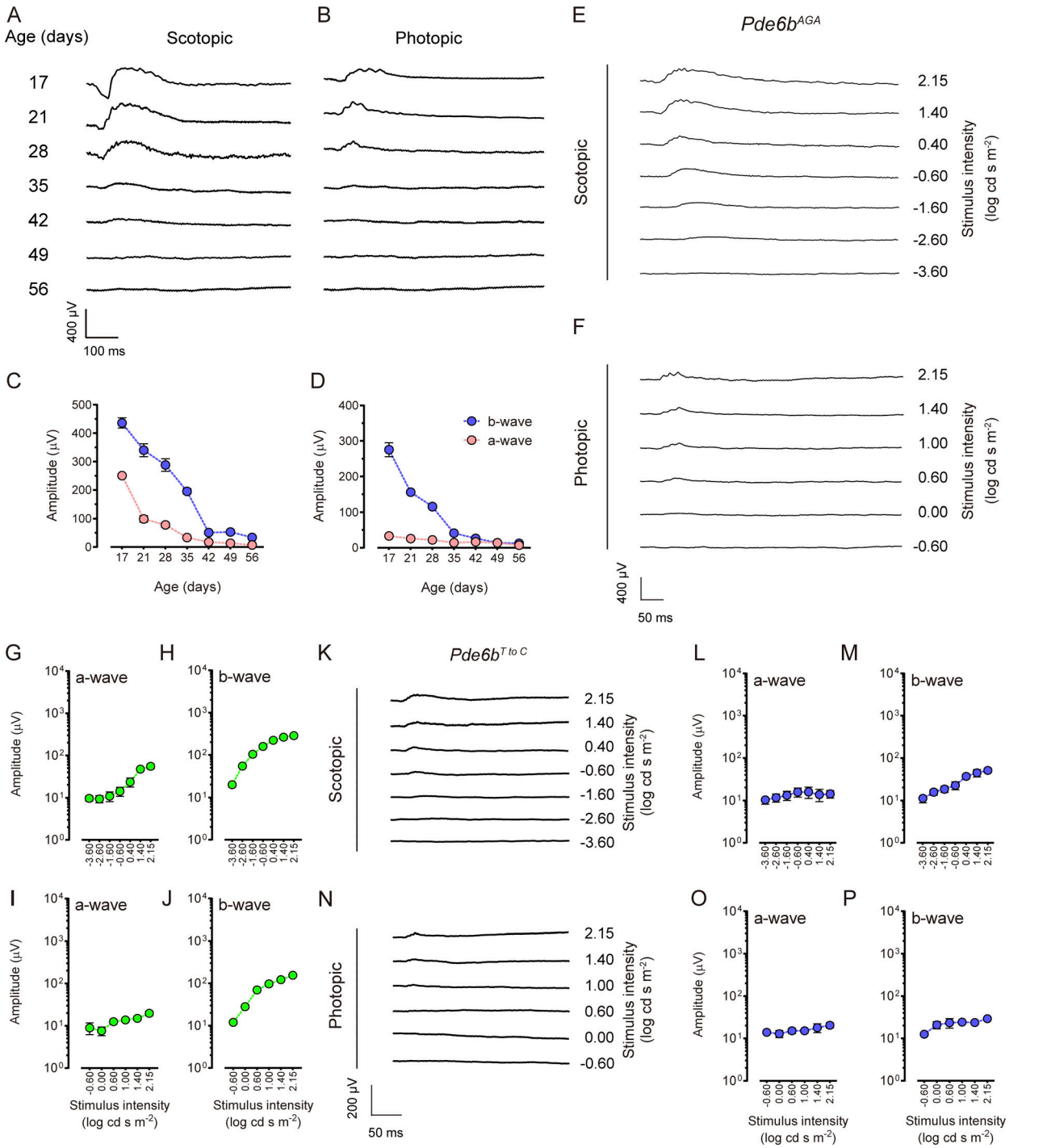

Figure S4. **ERG responses in *Pde6b*^{rd10} control mice at different ages, in *Pde6b*^{AGA} mice, and in the *Pde6b*^{rd10} mice treated at P21 with PE^{SpRY} system and g*Pde6b*. (A and B)** Representative scotopic (A) and photopic (D) ERG responses in the *Pde6b*^{rd10} mice at P17, 21, 28, 35, 42, 49, and 56. ERGs were recorded with the light intensities of 2.15 log cd s m^{-2} in both dark-adapted (A) and light-adapted mice (B). **(C and D)** The amplitudes of a- and b-wave were measured for scotopic (C) or photopic (D) ERG. Representative data are presented as mean ± SEM; *n* = 6 independent biological replicates. All experiments were independently performed at least three times to ensure repeatable results. **(E–J)** ERG responses are significantly improved in the *Pde6b*^{AGA} mice. Representative scotopic (E) and photopic (F) ERG responses in the *Pde6b*^{AGA} mice at P120. ERGs were recorded in dark-adapted mice (E) with the light intensities increasing from −3.6 to 2.15 log cd s m^{-2} and in light-adapted mice (F) from −0.6 to 2.15 log cd s m^{-2}. The amplitudes of a- (G and I) and b-wave (H and J) were measured for scotopic (G and H) or photopic (I and J) ERG. Representative data are presented as mean ± SEM; *n* = 6 independent biological replicates. All experiments were independently performed at least three times to ensure repeatable results. **(K–P)** ERG responses are mildly improved in the *Pde6b*$^{T\ to\ C}$ mice treated at P21. Representative scotopic (K) and photopic (N) ERG responses in the *Pde6b*$^{T\ to\ C}$ mice at P120. ERGs were recorded in dark-adapted mice (K) with the light intensities increasing from −3.6 to 2.15 log cd s m^{-2} and in light-adapted mice (N) from −0.6 to 2.15 log cd s m^{-2}. The amplitudes of a- (L and O) and b-wave (M and P) were measured for scotopic (L and M) or photopic (O and P) ERG. Representative data are presented as mean ± SEM; *n* = 6 independent biological replicates. All experiments were independently performed at least three times to ensure repeatable results.

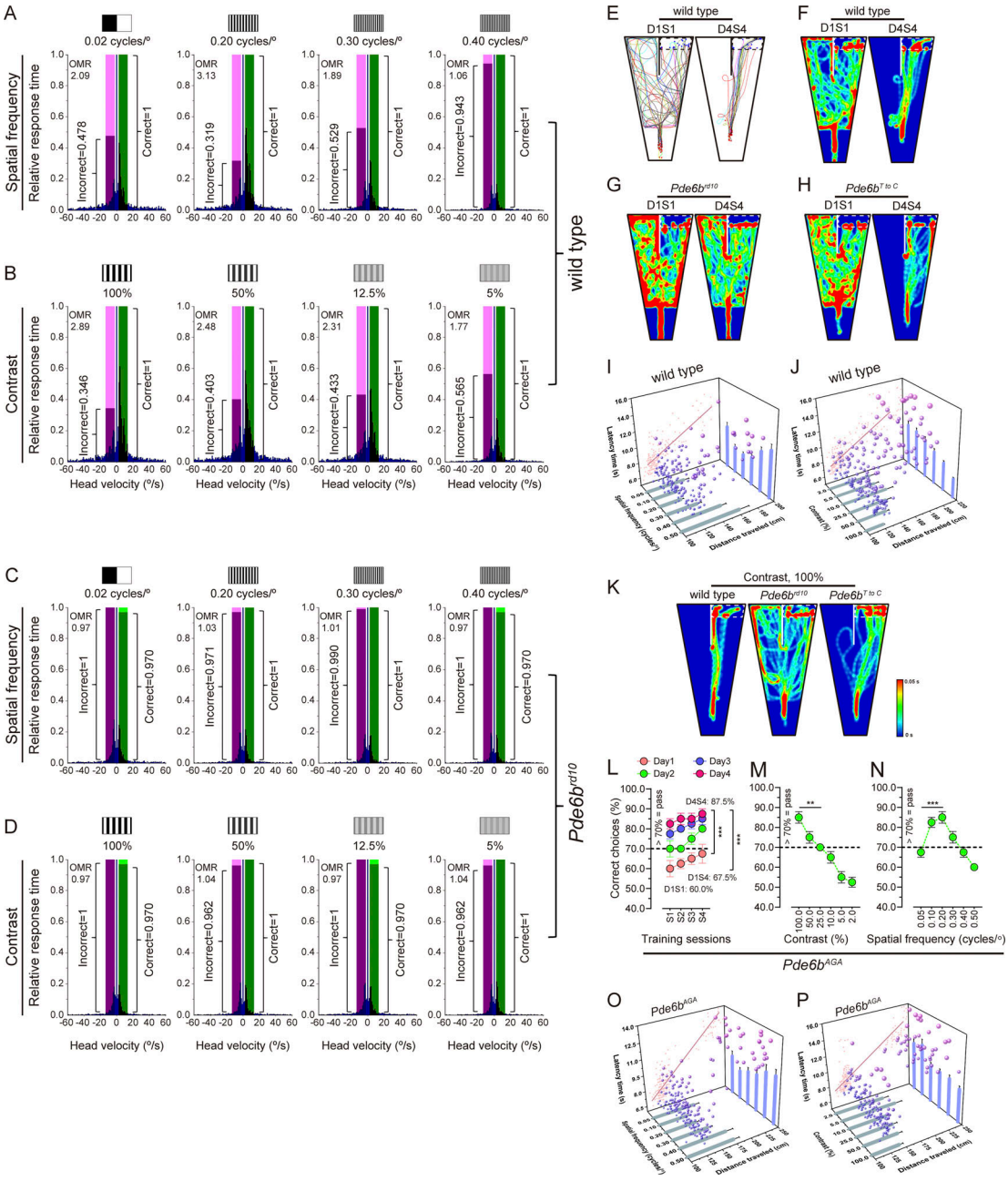

Figure S5. **The visual stimuli–driven optomotor responses in wild-type and *Pde6b*^{rd10} control mice, and mouse performance in water task. (A–D)** The visual stimuli–driven optomotor responses are significant in the wild-type (A and B) or not detectable in the *Pde6b*^{rd10} control contexts (C and D) when tested at defined spatial frequencies (A and C) or contrasts (B and D) under the optimal velocity conditions (2–14°/s). The response time in either stimulus direction (positive value, light green window) or opposite direction (negative value, light magenta window) at defined velocity thresholds is normalized to the maximal response time which is defined as 1 and presented as a blue bar. The OMR values at each spatial frequency or contrast are indicated with a magenta bar normalized to green one defined as 1 if the response time in the stimulus direction is longer than that in the opposite direction, and vice versa. Representative results are shown here. All of *Pde6b*^{rd10} control mice were treated with PE^{SpRY} and gScrambled. **(E–P)** Mouse performance in water task. **(E)** Representative traveling trajectories of wild-type mice during training sessions of D1S1 and D4S4. **(F–H)** Representative heat maps for the group-average of time traveled at distinct positions by wild-type (F), *Pde6b*^{rd10} control mice (G), and *Pde6b*$^{T\ to\ C}$ mice (H) during training sessions of D1S1 and D4S4. **(I and J)** Average swim latency time (cyan bars) and distance (blue bars) traveled of wild-type mice at different spatial frequencies (I) or contrasts (J). **(K)** Representative heat maps for the group-average of time traveled at distinct positions by wild-type, *Pde6b*^{rd10}, and *Pde6b*$^{T\ to\ C}$ mice under 100% of contrast level. **(L)** Pass rates of *Pde6b*^{AGA} mice during the training period for four consecutive days (D1–D4) with four sessions (S1–S4) each day. D1S1, D1S4, and D4S4 mean session 1 of day 1, session 4 of day 1 and session 4 of day 4, respectively. **(M and N)** Average pass rates of *Pde6b*^{AGA} mice at different spatial frequencies (M) or contrasts (N). **(O and P)** Average swim latency time (cyan bars) and distance traveled (blue bars) of *Pde6b*^{AGA} mice at different spatial frequencies (O) or contrasts (P). The coordinates of spheres are determined by latency time, distance traveled, and spatial frequency or contrast in each test. The sphere sizes indicate the amounts of latency time spent and the pink points are determined by latency time and distance traveled in each test. Representative data are presented as mean ± SEM, two-way ANOVA followed by Tukey's multiple comparisons test, $n \geq 4$ independent biological replicates. **, $P < 0.01$; ***, $P < 0.001$. All of *Pde6b*^{rd10} control mice were treated with PE^{SpRY} and gScrambled. All experiments were independently performed at least three times to ensure repeatable results.

Provided online are nine tables and two datasets. Table S1 shows sequences of p1–p14 gRNAs. Table S2 shows sequences of ngRNA n1–n7 and distance from the target T•A base pair. Table S3 shows sequences of pegRNAs for optimization of RT templates and PBS lengths. Table S4 shows sequences of pegRNAs for diverse editings with optimized RT templates and PBS. Table S5 shows sequences of pegRNAs and ngRNAs for PE^{SpCas9} genome editing. Table S6 shows sequences of pegRNAs for in vivo genome editing in *Pde6b*^{rd10} mice. Table S7 shows viral constructs, Rep/Cap, and virus titers. Table S8 shows primers used in the study. Table S9 shows antibodies used for immunohistochemistry and Western blotting. Data S1 shows sequences of indels for the pegRNA or ngRNA in the treated retinas. Data S2 show the sequences of constructs used in this study.